# EXPERIMENTAL STUDY OF THE ANISOTROPIC FLOW DEFORMATION AND CRITICAL STATE OF SAND

Ph.D. Dissertation, Geotechnical Division, N.T.U.A.

by

Panayiotis K. Triantafyllos

## EXTENDED ABSTRACT

This thesis investigates experimentally the mechanical behaviour of sand under triaxial and generalised loading. The anisotropic flow deformation and critical state of M31 Sand were investigated using the hollow cylinder apparatus and two triaxial apparatuses of the National Technical University of Athens, all of which were either updated or modified for the needs of the present study. Monotonic and cyclic loading was imposed on water pluviated sand specimens under a broad range of consolidation effective stresses, $p'_c = (\sigma'_{1c} + \sigma'_{2c} + \sigma'_{3c}) / 3$, and stress ratios, $K_c = \sigma'_{3c} / \sigma'_{1c}$, with fixed or rotating stress principal axes (PA) and with two different values of the intermediate principal stress parameter, $b = (\sigma'_2 - \sigma'_3) / (\sigma'_1 - \sigma'_3)$.

The results from monotonic triaxial compression tests indicate the existence of a unique critical state line in the $p' - e - q$ space for M31 Sand, irrespective of the initial value of void ratio and mean effective stress and drainage conditions. The state parameter, $\psi$, proposed by Been and Jefferies (1985) normalises the strength and dilatancy characteristics of sand while the stress – dilatancy relationship depends on state. The results from monotonic undrained loading tests at different fixed directions of the $\sigma'_1$-axis with respect to the vertical, measured by angle $\alpha_{\sigma'1}$, and with constant $p$ and $b$ showed that the inherent anisotropy affects the strength and deformability of isotropically consolidated sand at the instability point, phase transformation point and peak-failure state. The response of sand becomes, in general, more contractive and less stiff when the angle $\alpha_{\sigma'1}$ increases yet the weakest response is observed when one of the maximum stress obliquity planes tends to align at failure with the horizontal bedding plane. The same amount of shear strain or normalised excess pore-water pressure is accumulated in the contractive phase of response at a lower deviatoric stress ratio when $\alpha_{\sigma'1}$ is higher. Moreover, flow instability is triggered at a lower deviatoric stress ratio when $\alpha_{\sigma'1}$ is higher. Despite the fixity of the stress PA the deformation of sand is (weakly) non-coaxial up to the peak-failure state, becoming coaxial only after intense dilative straining post-peak, while the principal direction of incremental stain is biased towards $\alpha_{d\varepsilon 1}$ = +45°, possibly because sliding occurs more easily along the horizontal bedding plane.

Undrained loading tests were conducted on anisotropically consolidated sand with monotonically rotating stress PA at constant $p$ and $b$ and with either monotonically increasing, constant or cyclically changing deviatoric stress, $q$, in order to investigate the effect of consolidation and loading history on the mechanical behaviour of sand. It was found that the combinations of $\varphi = \sin^{-1} [(\sigma'_1 - \sigma'_3) / (\sigma'_1 + \sigma'_3)]$ and $\alpha_{\sigma'1}$ at the triggering of flow instability are not unique, albeit being stated differently in previous studies (Nakata et al. 1998, Sivathayalan and Vaid 2002). On the contrary, the triggering condition and deformation pattern of flow depend on the stress-strain history, including the effect of $K_c$ and incremental stress direction· a new flow parameter indicates this dependence. It was also shown that a small stress perturbation involving rotation of the stress PA can trigger flow when the sand is consolidated at low $K_c$. For higher values of $K_c$ the rotation of the stress PA at constant $q$ may still induce plastic contraction, flow instability and failure of sand. Apart from the effects of stress-strain history on bifurcation the inherent anisotropy also plays an important role since the triggering of both diffuse and localised instabilities occurs preferably at stress states corresponding to unfavourable deformation kinematics, i.e. to shearing and sliding along the horizontal bedding plane.

The rotation of the stress PA is associated with strong non-coaxiality that persists past the state of peak failure. Distinct non-coaxiality patterns and elastic-plastic coupling, associated with the unloading of the non-diagonal component of the stress tensor, were observed during the first cycles of stress rotation, at low deviatoric stress ratio, when the deviatoric stress was kept constant. The non-coaxiality angle, $\xi$, decreases with the deviatoric stress ratio in both non-coaxiality patterns, though, the sand ultimately deforms in a steady state corresponding to a stabilised angle of non-coaxiality, mean effective stress and deviatoric stress ratio, only to be arrested by the triggering of diffuse or localised instabilities. These non-coaxiality patterns are, in general, independent of the value of $K_c$ and the number of the previous stress rotation cycles and are also observed in the case that the deviatoric stress changes periodically. On the other hand, distinct non-coaxiality patterns are observed before peak failure depending on the value of $K_c$ when the rate of stress rotation decreases as the deviatoric stress increases, though, the differences become less pronounced past the peak-failure state. Interestingly, stronger non-coaxiality corresponds to a lower $K_c$ and the effect of pre-shearing on non-coaxiality appears to be more important than the effect of the rate of stress rotation, as has been previously pointed out by Gutierrez et al. (1991).

Among the novel findings of this study are those indicating that the stress state of loose sand subjected to undrained principal stress rotation at constant deviatoric stress may move along the direction of isotropic stress unloading from the consolidation state to the failure state without triggering flow. This behaviour is a contrast to the predictions of recent models developed within the framework of Bifurcation Theory which indicate that the direction of isotropic unloading belongs to the set of unstable directions of loose sand even at low deviatoric stress ratio, away from the peak failure state (Darve and Laouafa 2000, Darve et al. 2004, Sibille at al. 2007, Prunier et al. 2009). Once the failure surface has been reached it was shown that a quasi-static diffuse instability can be triggered under increasing effective stresses and decreasing stress ratio, followed by a dynamic diffuse instability under decreasing stresses and stress ratio. Consequently, the experimental results verify for the first time the predictions of the numerical analyses by Darve that instability may occur under increasing effective stresses and decreasing stress ratio (Darve and Laouafa 2000, Darve et al. 2004, Sibille at al. 2007, Prunier et al. 2009).

This study shows that sand exhibits strong non-coaxiality and contracts whenever the loading with fixed stress PA is interrupted by a continuous rotation of the stress PA. The degree of non-coaxiality and associated contractancy becomes higher when the previous shearing becomes more intense in terms of shear strain accumulation. The novel findings reported herein indicate that the influence of pre-shearing on sand's behaviour is more important than the influence of the degree of stress rotation and the level of $\eta$, $p'$, $e$ and $b$, reported in previous studies (Miura et al. 1986, Gutierrez et al. 1991, Li and Yu 2010, Tong et al. 2010 and 2014), but diminishes gradually as the stress rotation continues. Specifically, it is shown that sand exhibits strong non-coaxiality and contracts immediately upon initiating the rotation of the stress PA at constant effective stress principal values (PV) very close to critical state albeit it was previously dilating on the failure surface in a coaxial deformation mode, under radial loading; the phenomenon becomes increasingly intense as critical state is approached. Dafalias's (2016) thought experiment is the limiting case of the sequence of experiments performed herein thus the presented experimental evidence is supporting the claim that the Anisotropic Critical State Theory by Li and Dafalias (2012) constitutes a necessary revision of the classical Critical State Theory.

Accordingly, the effect of pre-shearing on the non-coaxiality and contractancy of highly-stressed sand is also apparent when undrained loading is imposed after anisotropic consolidation. In this case, a small stress perturbation involving rotation of the stress PA induces strong non-coaxiality and the associated plastic contraction triggers flow instability. This situation is the diffuse analogue of the mechanism in the incipient shear band described by Vardoulakis (Vardoulakis et al. 1978, Vardoulakis and Graf 1985, Vardoulakis and Georgopoulos 2005) and may explain the vulnerability of sands to spontaneous liquefaction, in stress-rotation conditions, when the static shear stress is high.

The results from this thesis offer new knowledge and contribute towards the deeper understanding of the effects of anisotropy and loading history on the mechanical behaviour of sand. The deposition process and loading history influence the formation and evolution of fabric and this microscopic process controls the macroscopic mechanical behaviour of sand at every state, including the critical one. Consequently, the necessity is highlighted to develop models that can simulate the effects of fabric on the mechanical behaviour of sand under generalised and complex loading conditions, similar to those imposed in the current study. The future research will be directed towards the application of techniques for measuring the fabric tensor of granular media by means of physical properties like the electrical conductivity and the mechanical wave velocity. Likewise, the investigation of the mechanical behaviour of sand under true triaxial loading conditions is an attractive subject for future research.

## ΒΙΒΛΙΟΓΡΑΦΙΑ (BIBLIOGRAPHY)

Arthur JRF, Menzies BK (1972) Inherent anisotropy in a sand. Géotechnique 22 (1), 115–129

Been K, Jefferies MG (1985) A state parameter for sands. Géotechnique 35 (2), 99–112

Been K, Jefferies MG, Hachey J (1991) The critical state of sands. Géotechnique 41 (3), 365–381

Borja RI (2006) Condition for liquefaction instability in fluid-saturated granular soils. Acta Geotechnica 2006; 1:211-224

Brewer R (1964) Fabric and mineral analysis of soils. John Wiley and Sons, Inc. pp. 129-158

Casagrande A, Carillo N (1944) Shear failure of anisotropic materials. Proc. Boston Soc. Civ. Engrs, 31, 74-87

Dafalias YF (1977) Elasto-plastic coupling within a thermodynamic strain space formulation of plasticity. Int. J. Non-Linear Mech., Vol. 12, pp. 327-337

Dafalias YF (2016) Must critical state theory be revisited to include fabric effects? Acta Geotechnica (2016) 11:479, DOI 10.1007/s11440-016-0441-0

Daouadji A, Darve F, Al Gali H, Hicher PY, Laouafa F, Lignon S, Nicot F, Nova R, Pinheiro M, Prunier F, Sibille L, Wan R (2011) Diffuse failure in geomaterials: Experiments, theory and modelling. Int. J. Numer. Anal. Meth. Geomech. (2011), 35(16), 1731-1773

Darve F, Flavigny M, Meghachou M (1995) Constitutive modelling and instabilities of soil behaviour. Computers and Geotechnics 17 (1995), 203-224

Darve F, Laouafa F (2000) Instabilities in granular materials and application to landslides. Mech. Cohes-Frict. Mater., 2000; 5:627-652

Darve F, Servant G, Laouafa F, Khoa HDV (2004) Failure in geomaterials: continuous and discrete analysis. Comput. Methods Appl. Mech. Engrg. 193 (2004), 3057-3085

Desrues J, Hammad W (1989) Shear banding dependency on mean stress level in sand. Numerical Methods for Localization and Bifurcation of Granular Bodies, International Workshop, Gdańsk-Sobieszewo, September 25-30, 1989

Desrues J, Chambon R, Mokni M, Mazerolle F (1996) Void ratio inside shear bands in triaxial sand specimens studied by computed tomography. Géotechnique 46 (3), 529-546

Desrues J, Viggiani G (2004) Strain localization in sand: an overview of the experimental results obtained in Grenoble using stereophotogrammetry. International Journal for Numerical and Analytical Methods in Geomechanics, 2004, 28: 279-321

Desrues J, Georgopoulos I-O (2006) An investigation of diffuse failure modes in undrained triaxial tests on loose sand. Soils and Foundations, Vol.46, No.5, 585-594

Fu P, Dafalias YF (2011) Fabric evolution within shear bands of granular materials and its relation to critical state theory. International Journal for Numerical and Analytical Methods in Geomechanics, 2011, 35: 1918-1948

Georgiannou VN, Konstadinou M (2014) Torsional shear behavior of anisotropically consolidated sands. J. Geotech. Geoenviron. Eng., ASCE 140 (2), ISSN: 1090-0241/04013017(14)

Gong G, Thornton C, Chan AHC (2012) DEM simulations of undrained triaxial behavior of granular material. Journal of Engineering Mechanics, Vol. 138, No 6, 560-566

Guo N, Zhao J (2013) The signature of shear-induced anisotropy in granular media. Computers and Geotechnics, 47, 1-15

Gutierrez M, Ishihara K, Towhata I (1991) Flow theory for sand during rotation of principal stress direction. Soils and Foundations, Vol.31, No.4, pp. 121-132

Hight DW, Gens A, Symes MJ (1983) The development of a new hollow cylinder apparatus for investigating the effects of principal stress rotation in soils. Géotechnique 33, No. 4, 355-383

Hill R (1958) A general theory of uniqueness and stability in elastic-plastic solids. Journal of the Mechanics and Physics of Solids (1958); 6:239-249

Hu M, O'Sullivan C, Jardine RR, Jiang M (2010) Stress-induced anisotropy in sand under cyclic loading. Granular Matter, 12: 469-476

Hueckel T (1976) Coupling of elastic and plastic deformation of bulk solids. Mechanica 11:227–235

Ishihara K, Tatsuoka F, Yasuda S (1975) Undrained deformation and liquefaction of sand under cyclic stresses. Soils and Foundations, Vol.15, No.1, 29-44

Ishihara K, Towhata I (1983) Sand response to cyclic rotation of principal stress directions as induced by wave loads. Soils and Foundations, Vol.23, No.4, 11-26

Ishihara K (1993) Liquefaction and flow failure during earthquake. Géotechnique, Vol. 43, No. 3, pp.351-415

Lade PV, Nelson RB, Ito YM (1988) Instability of granular materials with nonassociated flow. Journal of Engineering Mechanics, Vol. 114, No. 12, 2173-2191

Lade PV (1993) Initiation of static instability in the submarine Nerlerk berm. Canadian Geotechnical Journal 30: 895-904

Lam WK, Tatsuoka F (1988) Effects of initial anisotropic fabric and $\sigma_2$ on strength and deformation characteristics of sand. Soils and Foundations, Vol.28, No.1, pp. 89-106

Li XS, Wang Y (1998) Linear representation of steady-state line for sand. J. Geotech. Geoenviron. Eng., 124(12), 1215-1217

Li XS, Dafalias YF (2000) Dilatancy for cohesionless soils. Géotechnique 50, No. 4, 449-460

Li X, Li XS (2009) Micro-macro quantification of the internal structure of granular materials. J. Eng. Mech., 135(7), 641-656

Li X, Yu H-S (2010) Numerical investigation of granular material behaviour under rotational shear. Géotechnique 60, No. 5, 381-394

Li XS, Dafalias YF (2012) Anisotropic critical state theory: role of fabric. Journal of Engineering Mechanics, Vol. 138, No. 3, 263-275

Li X, Yang D, Yu H-S (2016) Macro deformation and micro structure of 3D granular assemblies subjected to rotation of principal stress axes. Granular Matter (2016) 18:53, DOI: 10.1007/s10035-016-0632-2

Lü X, Huang M, Qian J (2018) Influences of loading direction and intermediate principal stress ratio on the initiation of strain localization in cross-anisotropic sand. Acta Geotech., 13: 619-633, 2018

Manzari MT, Dafalias YF (1997) A critical state two-surface plasticity model for sands. Géotechnique 47, No. 2, 255-272

Masson S, Martinez J (2001) Micromechanical analysis of the shear behavior of a granular material. J. Eng. Mech., 127(10), 1007-1016

Miura K, Miura S, Toki S (1986) Deformation behavior of anisotropic dense sand under principal stress axes rotation. Soils and Foundations, Vol.26, No.1, 36-52

Nakata Y, Hyodo M, Murata H, Yasufuku N (1998) Flow deformation of sands subjected to principal stress rotation. Soils and Foundations, Vol.38, No.2, 115-128

Nicot F, Darve F (2011) Diffuse and localized failure modes: Two competing mechanisms. International Journal for Numerical and Analytical Methods in Geomechanics, Vol. 35, 586-601

Nova R (1994) Controllability of the incremental response of soil specimens subjected to arbitrary loading programmes. Journal of the Mechanical Behavior of Materials, 5(2):193-201

Oda M (1972) Initial fabrics and their relations to mechanical properties of granular material. Soils and Foundations, Vol.12, No.1, 18-36

Oda M, Nemat-Nasser S, Konishi J (1985) Stress-induced anisotropy in granular masses. Soils and Foundations, Vol.25, No.3, 85-97

Poulos SJ, Castro G, France JW (1985) Liquefaction evaluation procedure. Journal of Geotechnical Engineering, ASCE, Vol.111, No.6, pp. 772-792

Prunier F, Nicot F, Darve F, Laouafa F, Lignon S (2009) Three-dimensional multiscale bifurcation analysis of granular media. Journal of Engineering Mechanics, Vol. 135, No. 6, 493-509

Roscoe KH, Schofield AN, Wroth CP (1958) On the yielding of soils. Géotechnique 8 (1), 22–53

Roscoe KH (1970) The influence of strains in soil mechanics. Tenth Rankine Lectrure, Géotechnique 20, No. 2, 129-17

Salvatore E, Mondoni G, Ando E, Albano M, Viggiani G (2017) Determination of the critical state of granular materials with triaxial tests. Soils Found. (2017), https://doi.org/10.1016/j.sandf.2017.08.005

Sasitharan S, Robertson PK, Sego DC, Morgenstern NR (1993) Collapse behavior of sand. Can. Geotech. J. 30, 569-577

Satake M (1978) Constitution of mechanics of granular materials through graph representation. Theoretical and Applied Mechanics 26, University of Tokyo Press, pp. 257-266

Schofield AN, Wroth CP (1968) Critical state soil mechanics. McGraw-Hill, London

Shibuya S, Hight DW (1987) A bounding surface of granular materials. Soils and Foundations, Vol.27, No.4, 123-136

Shibuya S, Hight DW, Jardine RJ (2003a) Four-dimensional local boundary surfaces of an isotropically consolidated loose sand. Soils and Foundations, Vol.43, No.2, 89-103

Shibuya S, Hight DW, Jardine RJ (2003b) Local boundary surfaces of a loose sand dependent on consolidation path. Soils and Foundations, Vol.43, No.3, 85-93

Sibille L, Nicot F, Donzé FV, Darve F (2007) Material instability in granular assemblies from fundamentally different models. Int. J. Numer. Anal. Meth. Geomech., 2007; 31:457–481

Sivathayalan S, Vaid YP (2002) Influence of generalized initial state and principal stress rotation on the undrained response of sands. Canadian Geotechnical Journal, 39 (1): 63 – 76

Symes MJ, Gens A, Hight DW (1984) Undrained anisotropy and principal stress rotation in saturated sand. Géotechnique 34, No. 1, 11-27

Tatsuoka F, Ishihara K (1974) Drained deformation of sand under cyclic stresses reversing direction. Soils and Foundations, Vol.14, No.3, pp. 51-65

Theocharis AI, Vairaktaris E, Dafalias YF, Papadimitriou AG (2017) Proof of incompleteness of Critical State Theory in granular mechanics and its remedy. Journal of Engineering Mechanics, Vol. 143 (2), 1-12

Theocharis AI, Vairaktaris E, Dafalias YF, Papadimitriou AG (2019) Necessary and sufficient conditions for reaching and maintaining critical state. International Journal for Numerical and Analytical Methods in Geomechanics, 43: 2041-2045

Thornton C (2000) Numerical simulations of deviatoric shear deformation of granular media. Géotechnique 50, No. 1, 43-53

Tong Z, Zhang J, Yu Y, Ga Zhang (2010) Drained deformation behavior of anisotropic sands during cyclic rotation of principal stress axes. Journal of Geotechnical and Geoenvironmental Engineering, Vol. 136, No.11, pp. 1509-1518

Tong Z, Fu P, Dafalias YF, Yao Y (2014) Discrete element method analysis of non-coaxial flow under rotational shear. Int. J. Numer. Anal. Meth. Geomech., 2014; 38:1519–1540

Triantafyllos PK, Georgiannou VN, Dafalias YF, Georgopoulos I-O (2019) New findings on the evolution of the instability surface of loose sand. Acta Geotechnica, https://doi.org/10.1007/s11440-019-00887-7

Triantafyllos PK, Georgiannou VN, Pavlopoulou EM, Dafalias YF (2020) Strength and dilatancy of sand before and after stabilisation with colloidal-silica gel. Géotechnique (under review)

Tsomokos A (2005) Experimental study of the behaviour of a soil element under monotonic and cyclic torsional shear. PhD Thesis, National Technical University of Athens

Vaid YP, Chern JC (1983) Effect of static shear on resistance to liquefaction. Soils and Foundations, Vol.23, No.1, pp. 47-60

Vardoulakis I, Goldscheider M, Gudehus G (1978) Formation of shear bands in sand bodies as a bifurcation problem. International Journal for Numerical and Analytical Methods in Geomechanics, 1978, 2: 99-128

Vardoulakis I, Graf B (1985) Calibrations of constitutive models for granular materials using data from biaxial experiments. Géotechnique 35, No. 3, 299-317

Vardoulakis I, Sulem J (1995) Bifurcation analysis in geomechanics. Chapman and Hall, 1995

Vardoulakis I, Georgopoulos I-O (2005) The “stress-dilatancy” hypothesis revisited: shear-banding related instabilities. Soils and Foundations, Vol.45, No.2, pp. 61-76

Verdugo R, Ishihara K (1996) The steady state of sandy soils. Soils and Foundations, Vol.36, No.2, pp. 81-91

Wang R, Fu P, Zhang J-M, Dafalias YF (2017) Evolution of various fabric tensors for granular media toward the critical state. J. Eng. Mech., 2017, 143(10): 04017117

Wiebicke M, Andò E, Salvatore E, Viggiani G, Herle I (2017) Experimental measurement of granular fabric and its evolution under shearing. Powders and Grains (2017), EPJ Web of Conferences. 140. 02020. 10.1051/epjconf/201714002020.

Wroth CP, Basset RH (1965) A stress-strain relationship for the shearing behaviour of a sand. Géotechnique 15, No. 1, 32-56

Yang ZX, Li XS, Yang J (2007) Undrained anisotropy and rotational shear in granular soil. Géotechnique 57, No. 4, 371-384

Yoshimine M, Ishihara K, Vargas W (1998): Effects of principal stress direction and intermediate principal stress on undrained shear behavior of sand. Soils and Foundations, Vol. 38, No. 3, 179-188

Yoshimine M, Ishihara K (1998) Flow potential of sand during liquefaction. Soils and Foundations, Vol. 38, No. 3, 189-198

Zhang L, Thornton C (2007) A numerical examination of the direct shear test. Géotechnique 57, No. 4, 343-354

Zhou W, Liu J, Ma G, Chang X (2017) Three-dimensional DEM investigation of critical state and dilatancy behaviors of granular materials. Acta Geotechnica (2017) 12:527-540

## ΠΙΝΑΚΕΣ (TABLES)

**Πίνακας 1** Κατάλογος των συμβόλων και των εξισώσεων που χρησιμοποιήθηκαν για τον υπολογισμό των μέσων τάσεων, παραμορφώσεων και άλλων παραμέτρων στις δοκιμές στρεπτικής διάτμησης

**Table 1** List of symbols and equations used to calculate the average stresses, strains and other parameters in torsional-shear tests

| Direction HC | Stress | Strain |
|---|---|---|

| | | |
|---|---|---|
| **Vertical** | $\sigma_{zz} = \frac{F}{\pi\left(r_o^2 - r_i^2\right)} + \frac{p_o r_o^2 - p_i r_i^2}{r_o^2 - r_i^2}$ | $\varepsilon_{zz} = -\frac{v_H}{H}$ |
| **Circumferential** | $\sigma_{\theta\theta} = \frac{p_o r_o - p_i r_i}{r_o - r_i}$ | $\varepsilon_{\theta\theta} = \frac{(\varepsilon_{vol} - \varepsilon_{zz})}{2}$ **or** $\varepsilon_{\theta\theta} = \varepsilon_{vol} - \varepsilon_{zz}$ |
| **Radial** | $\sigma_{rr} = \frac{p_o r_o + p_i r_i}{r_o + r_i}$ | $\varepsilon_{rr} = \frac{(\varepsilon_{vol} - \varepsilon_{zz})}{2}$ **or** $\varepsilon_{rr} = 0$ |
| **Rotational** | $\tau_{z\theta} = \frac{3T}{2\pi(r_o^3 - r_i^3)}$ | $\gamma_{z\theta} = 2\varepsilon_{z\theta} = \frac{2\theta\left(r_o^3 - r_i^3\right)}{3H(r_o^2 - r_i^2)}$ |
| **Principal** | **Stress** | **Strain** |
| **Major** | $\sigma_1 = \frac{\sigma_{zz} + \sigma_{\theta\theta}}{2} + \sqrt{\left(\frac{\sigma_{zz} - \sigma_{\theta\theta}}{2}\right)^2 + \tau_{z\theta}^2}$ | $\varepsilon_1 = \frac{\varepsilon_{zz} + \varepsilon_{\theta\theta}}{2} + \sqrt{\left(\frac{\varepsilon_{zz} - \varepsilon_{\theta\theta}}{2}\right)^2 + \varepsilon_{z\theta}^2}$ |
| **Intermediate** | $\sigma_2 = \sigma_{rr}$ | $\varepsilon_2 = \varepsilon_{rr}$ |
| **Minor** | $\sigma_3 = \frac{\sigma_{zz} + \sigma_{\theta\theta}}{2} - \sqrt{\left(\frac{\sigma_{zz} - \sigma_{\theta\theta}}{2}\right)^2 + \tau_{z\theta}^2}$ | $\varepsilon_3 = \frac{\varepsilon_{zz} + \varepsilon_{\theta\theta}}{2} - \sqrt{\left(\frac{\varepsilon_{zz} - \varepsilon_{\theta\theta}}{2}\right)^2 + \varepsilon_{z\theta}^2}$ |
| **Invariant** | **Stress** | **Strain** |
| | $q = (\frac{1}{2}\{(\sigma_1 - \sigma_2)^2 + (\sigma_2 - \sigma_3)^2 + (\sigma_3 - \sigma_1)^2\})^{1/2}$ | $\gamma = (\frac{2}{9}\{(\varepsilon_1 - \varepsilon_2)^2 + (\varepsilon_2 - \varepsilon_3)^2 + (\varepsilon_3 - \varepsilon_1)^2\})^{1/2}$ |
| | $p' = \frac{\sigma_1' + \sigma_2' + \sigma_3'}{3} = \frac{\sigma_1 + \sigma_2 + \sigma_3}{3} - u$ | $\varepsilon_{vol} = \varepsilon_1 + \varepsilon_2 + \varepsilon_3 \ (= \frac{-\Delta V}{V})$ |
| | $\tau_{oct} = \frac{1}{3}(\{(\sigma_1 - \sigma_2)^2 + (\sigma_2 - \sigma_3)^2 + (\sigma_3 - \sigma_1)^2\})^{1/2}$ | $\gamma_{oct} = \frac{2}{3}(\{(\varepsilon_1 - \varepsilon_2)^2 + (\varepsilon_2 - \varepsilon_3)^2 + (\varepsilon_3 - \varepsilon_1)^2\})^{1/2}$ |

| Parameters | Stress | Strain |
| --- | --- | --- |
| **Difference** | $q_d = \sigma_1 - \sigma_3$ | |
| | $X = \dfrac{\sigma'_{zz} - \sigma'_{\theta\theta}}{\sigma'_{zz} + \sigma'_{\theta\theta}}$, $X_s = \sigma'_{zz} - \sigma'_{\theta\theta}$ | $X_\varepsilon = \dfrac{\varepsilon_{zz} - \varepsilon_{\theta\theta}}{2}$ |
| | $Y = \dfrac{2\tau_{z\theta}}{\sigma'_{zz} + \sigma'_{\theta\theta}}$, $Y_s = 2\tau_{z\theta}$ | $Y_\varepsilon = \varepsilon_{z\theta}$ |
| **Direction of major principal stress/strain** | $\alpha \equiv \alpha_{\sigma'1} = 0.5 \cdot \tan^{-1}\dfrac{Y}{X} = $ $= 0.5 \cdot \tan^{-1}\dfrac{Y_s}{X_s}$ | $\alpha_{\varepsilon 1} = 0.5 \cdot \tan^{-1}\dfrac{Y_\varepsilon}{X_\varepsilon}$ |
| **Direction of major principal incremental stress/strain** | $\alpha_{d\sigma'1} = 0.5 \cdot \tan^{-1}\dfrac{dY_s}{dX_s}$ | $\alpha_{d\varepsilon 1} = 0.5 \cdot \tan^{-1}\dfrac{dY_\varepsilon}{dX_\varepsilon}$ |
| **Ratio** | $b = \dfrac{\sigma'_2 - \sigma'_3}{\sigma'_1 - \sigma'_3}$ | |
| **Ratio** | $\sin\varphi = \dfrac{\sigma'_1 - \sigma'_3}{\sigma'_1 + \sigma'_3}$ | |
| **Ratio** | $\eta = \dfrac{q}{p'}$ | |
| **Ratio** | $K_c = \dfrac{\sigma'_{3c}}{\sigma'_{1c}}$ | |
| **Second-order work** | $d^2W = (d\sigma_{zz} - d\sigma_{\theta\theta})(\dfrac{d\varepsilon_{zz} - d\varepsilon_{\theta\theta}}{2}) + 2d\tau_{z\theta}d\varepsilon_{z\theta}$, for isochoric conditions under b=0.5 | |
| **Normalised second-order work** | $d^2W_{norm} = d^2W / \left[\sqrt{(d\sigma_{zz} - d\sigma_{\theta\theta})^2 + (2d\tau_{z\theta})^2} \cdot \sqrt{(\dfrac{d\varepsilon_{zz} - d\varepsilon_{\theta\theta}}{2})^2 + (d\varepsilon_{z\theta})^2}\right]$, for isochoric conditions under b=0.5 | |
| **Angle between the σ'₁-axis and the planes of max(τ/σₙ')** | $\theta_{1,2} = \pm(45° - \varphi_{mob} / 2)$ | |

**Πίνακας 2** Κατάλογος των βασικών συμβόλων και συντομογραφιών

**Table 2** Notations and abbreviations

$\alpha$ material constant used in the relationship of the critical state line in the $e - (p'/p_a)^\alpha$ plane

$\varepsilon_1$ major principal strain

$\varepsilon_2$ intermediate principal strain

$\varepsilon_3$ minor principal strain

$\varepsilon_q$ deviatoric strain, $\varepsilon_q = 2^{1/2}/3[(\varepsilon_1 - \varepsilon_2)^2 + (\varepsilon_2 - \varepsilon_3)^2 + (\varepsilon_3 - \varepsilon_1)^2]^{1/2}$

$\varepsilon_{vol}$ volumetric strain, $\varepsilon_{vol} = \varepsilon_1 + \varepsilon_2 + \varepsilon_3$

$\eta$ stress ratio, $\eta = q/p'$

$\lambda$ slope of the critical state line in the $e - (p'/p_a)^\alpha$ plane

$\xi$ non-coaxiality angle, $\xi = \alpha_{d\varepsilon 1} - \alpha_{\sigma' 1}$

$\sigma'_1$ major effective principal stress

$\sigma'_2$ intermediate effective principal stress

$\sigma'_3$ minor effective principal stress

$\varphi$ angle of shearing resistance (degrees)

$\varphi_c$ angle of shearing resistance at the critical state (degrees)

$\psi$ state parameter of Been and Jefferies, $\psi = e - e_c(p')$

ACST anisotropic critical state theory

$B$ Skempton's pore-pressure coefficient

$c$ cohesion

CSL critical state line in the $e - p'$ plane

CST critical state theory

$D$ dilatancy ratio, $D = d\varepsilon^p_{vol} / d\varepsilon^p_q$ (the superscript p stands for plastic)

$e$ void ratio, $e = V_v / V_s$

$e_c(p')$ void ratio at the critical state at mean effective stress $p'$

$e_\Gamma$ material constant indicating the intercept of the critical state line in the $e - (p'/p_a)^\alpha$ plane with the $p' = 0$ axis

HCA  hollow cylinder apparatus

IP  instability point

IS  instability surface

$M$  stress ratio, $q$ / $p'$, at the critical state

PA  principal axes

PTP  phase-transformation point

PV  principal values

$p'$  mean effective stress, $p' = (\sigma'_1 + \sigma'_2 + \sigma'_3) / 3$

$p_a$  atmospheric pressure at zero elevation (101 kPa)

$q$  deviatoric stress, $q = [1/2((\sigma'_1 - \sigma'_2)^2 + (\sigma'_2 - \sigma'_3)^2 + (\sigma'_3 - \sigma'_1)^2)]^{1/2}$

$u$  pore-water pressure in excess of atmospheric pressure

$V_s$  volume of sand particles

$V_v$  volume of voids

**Πίνακας 3** Φυσικά χαρακτηριστικά της άμμου M31

**Table 3** Physical characteristics of M31 Sand

| | |
|---|---|
| **Specific gravity, $G_s$ (-):** | 2.66 |
| **Minimum void ratio, $e_{min}$ (-):** | 0.50 |
| **Maximum void ratio, $e_{max}$ (-):** | 0.80 |
| **Grain size $D_{10}$ (mm):** | 0.214 |
| **Grain size $D_{30}$ (mm):** | 0.258 |
| **Grain size $D_{50}$ (mm):** | 0.310 |
| **Grain size $D_{60}$ (mm):** | 0.339 |
| **Coefficient of uniformity, $C_u$ (-):** | 1.58 |
| **Coefficient of curvature, $C_h$ (-):** | 0.92 |

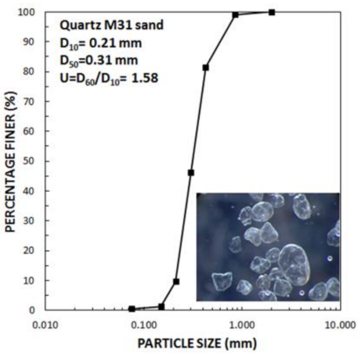


$D_p$ is the grain size (diameter) corresponding to $p$% finer in the grain size distribution curve. The coefficient of uniformity is $C_u = D_{60} / D_{10}$ while the coefficient of curvature is $C_h = (D_{30})^2 / (D_{60}*D_{10})$

**Πίνακας 4** Παράμετροι κρίσιμης κατάστασης της άμμου M31

**Table 4** Critical-state parameters of M31 Sand

| $e_c(p') = e_\Gamma - \lambda(p'/p_a)^\alpha$, $p_a$=101 kPa and $\eta_c = (q / p')_c = M$ | | | | |
|---|---|---|---|---|
| | $e_\Gamma$ | $\lambda$ | **α** | ***M* (for *b* = 0)** |

| | | | | |
|---|---|---|---|---|
| **M31 Sand** | 0.7682 | 0.0112 | 0.70 | 1.24 |

**Πίνακας 5** Συνθήκες κατά την έναρξη της στροφής των κύριων αξόνων τάσεως στις δοκιμές τύπου PAR

**Table 5** Conditions at the initiation of stress rotation in PAR-series tests

| **Test** | ***η*** **(-)** | ***p'*** **(kPa)** | ***b*** **(-)** | ***α*** **(°)** | $\varepsilon_q$ **(%)** | ***e*** **(-)** | ***ψ*** **(-)** | **Pre-shearing** |
|---|---|---|---|---|---|---|---|---|
| PAR1 | 1.01 | 100 | 0 | 0 | 0.78 | 0.693 | -0.064 | AC |
| PAR2 | 1.02 | 507 | 0.5 | 15 | 12.4 | 0.726 | -0.008 | RL |
| PAR3 | 1.05 | 343 | 0.5 | 15 | 7.6 | 0.744 | 0.003 | RL |
| PAR4 | 1.12 | 402 | 0.5 | 15 | 4.7 | 0.733 | -0.006 | RL |

# ΣΧΗΜΑΤΑ (FIGURES)

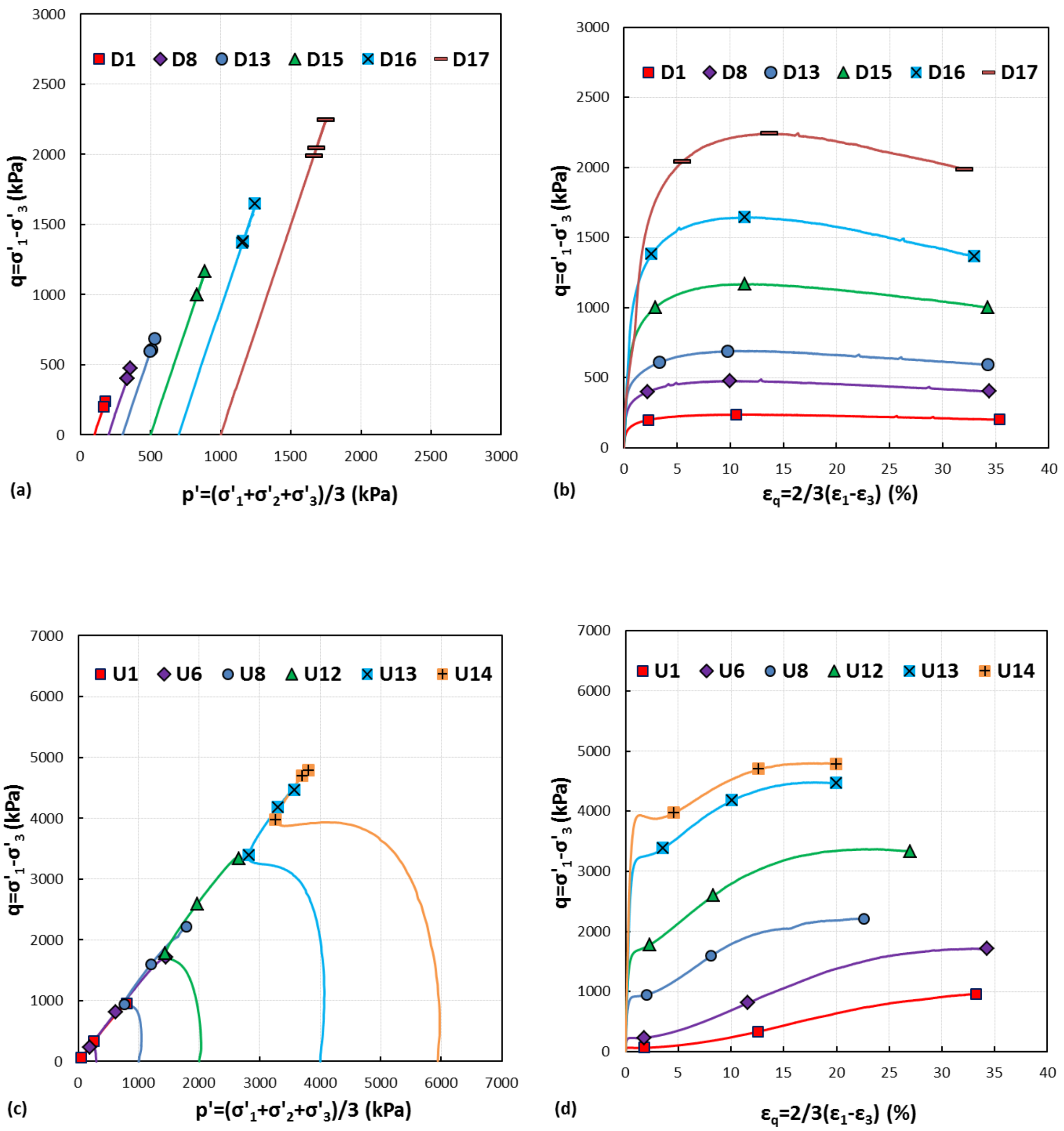


**Σχ. 1** Απόκριση ισότροπα στερεοποιημένης άμμου σε μονοτονική τριαξονική συμπίεση υπό στραγγιζόμενες (**a** & **b**) και αστράγγιστες (**c** & **d**) συνθήκες. **a** & **b** Ενεργές τασικές οδεύσεις στο $q-p'$ επίπεδο. **c** & **d** Καμπύλες αποκλίνουσας τάσης – παραμόρφωσης $(q-\varepsilon_q)$

**Fig. 1** Response of IC sand to monotonic triaxial compression under drained (**a** & **b**) and undrained (**c** & **d**) conditions. **a** & **b** Effective stress paths in the $q-p'$ plane. **c** & **d** Deviatoric stress – strain curves $(q-\varepsilon_q)$

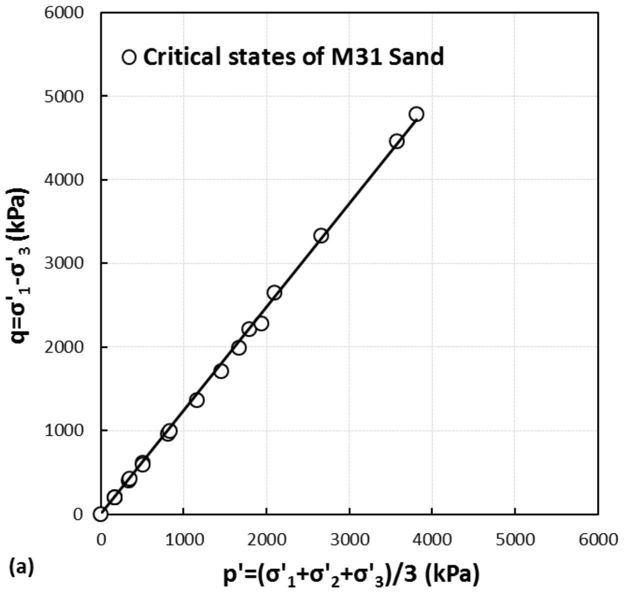


**Σχ. 2** Προβολή της Γραμμής Κρίσιμης Κατάστασης της άμμου Μ31 στο $q - p'$ επίπεδο τάσεων (**a**) και στο $e - p'$ καταστατικό επίπεδο (**b**)

**Fig. 2** Projection of the Critical State Line of M31 Sand in the $q - p'$ stress plane (**a**) and in the $e - p'$ state diagram (**b**)

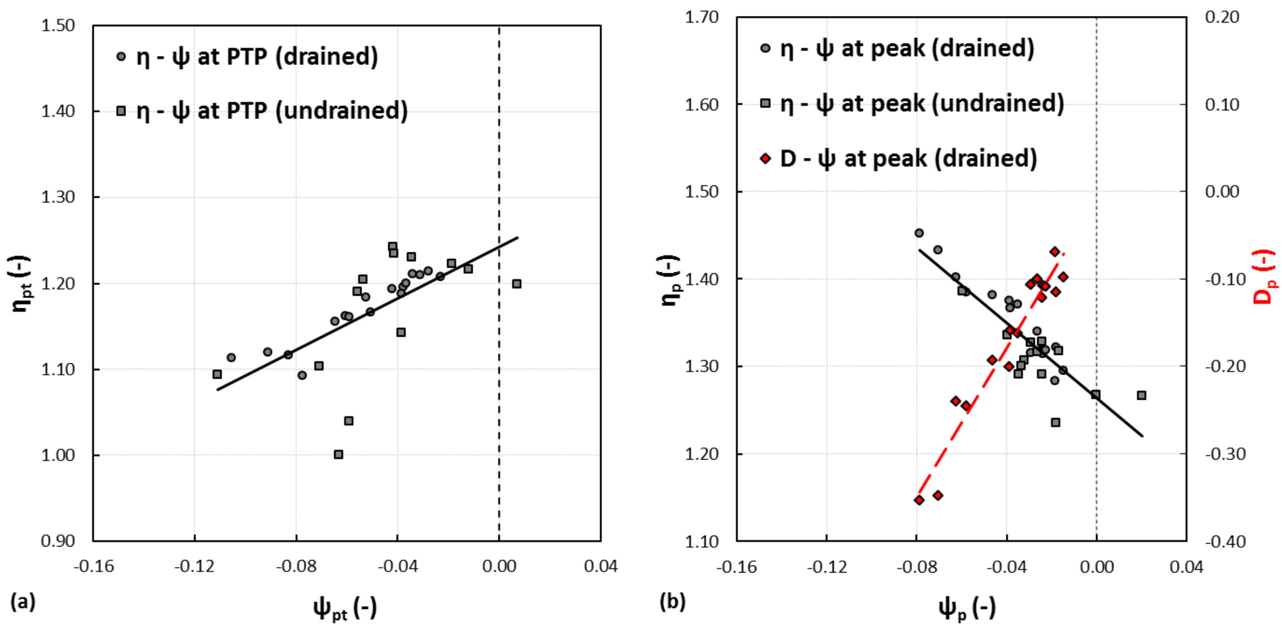


**Σχ. 3** Λόγος τάσεων, $\eta$, σε συνάρτηση με την καταστατική παράμετρο, $\psi$, στο σημείο αλλαγής φάσης (**a**) και λόγος τάσεων, $\eta$, και λόγος διαστολικότητας, $D$, σε συνάρτηση με την καταστατική παράμετρο, $\psi$, στην κατάσταση κορυφαίας αστοχίας (**b**)

**Fig. 3** Stress ratio, $\eta$, against the state parameter, $\psi$, at phase transformation point (**a**) and stress ratio, $\eta$, and dilatancy ratio, $D$, against the state parameter, $\psi$, at peak failure state (**b**)

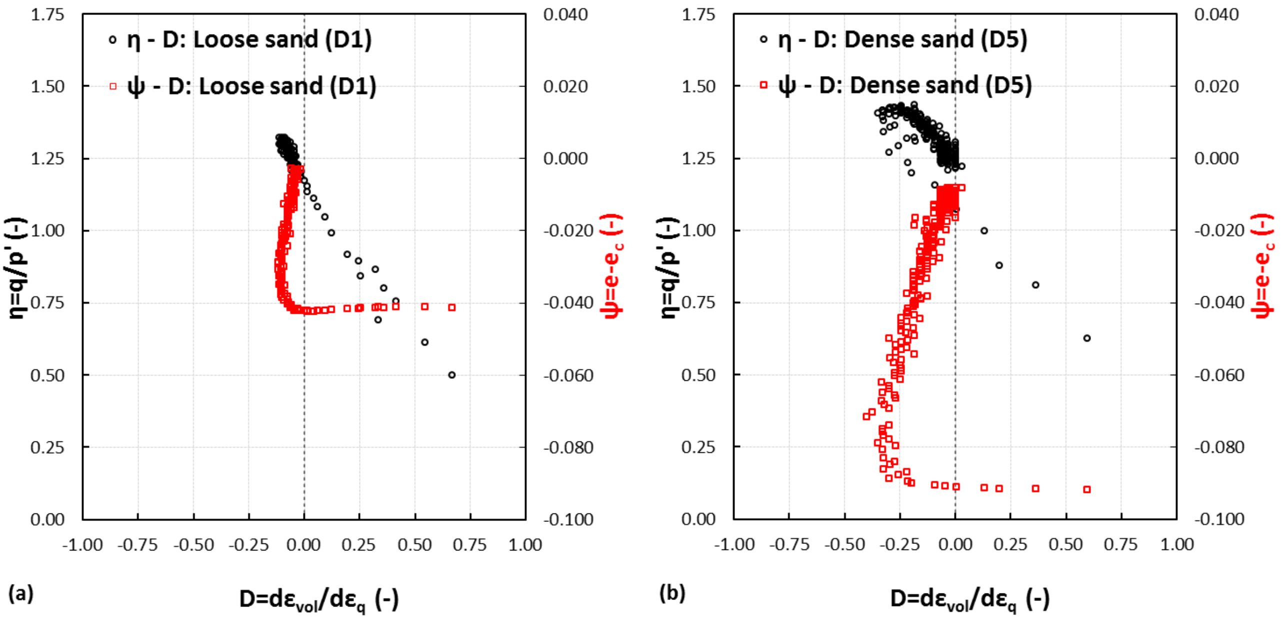


**Σχ. 4** Σχέση λόγου τάσεων – διαστολικότητας, $\eta - D$, και εξέλιξη της καταστατικής παραμέτρου, $\psi$, σε συνάρτηση με τον λόγο διαστολικότητας, $D$, για χαλαρή (**a**) και πυκνή άμμο (**b**)

**Fig. 4** Stress – dilatancy relationship, $\eta - D$, and evolution of state parameter, $\psi$, with the dilatancy ratio, $D$, for loose (**a**) and dense sand (**b**)

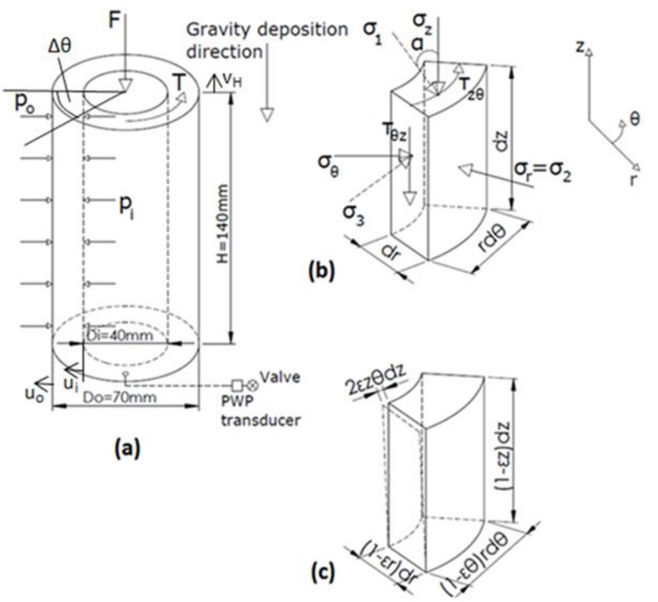


**Σχ. 5** **a** Κοίλο κυλινδρικό δοκίμιο και επιβαλλόμενα συνοριακά φορτία. **b** Συνιστώσες τάσεως στο μη παραμορφωμένο εδαφικό στοιχείο. **c** Συνιστώσες παραμορφώσεως αντιστοιχούσες σε συνδυασμό πολύ-αξονικής και στρεπτικής παραμόρφωσης

**Fig. 5** **a** Hollow-cylinder specimen and applied boundary loads. **b** Stress components on the undeformed soil element. **c** Strain components associated with the combined multiaxial and torsional deformation

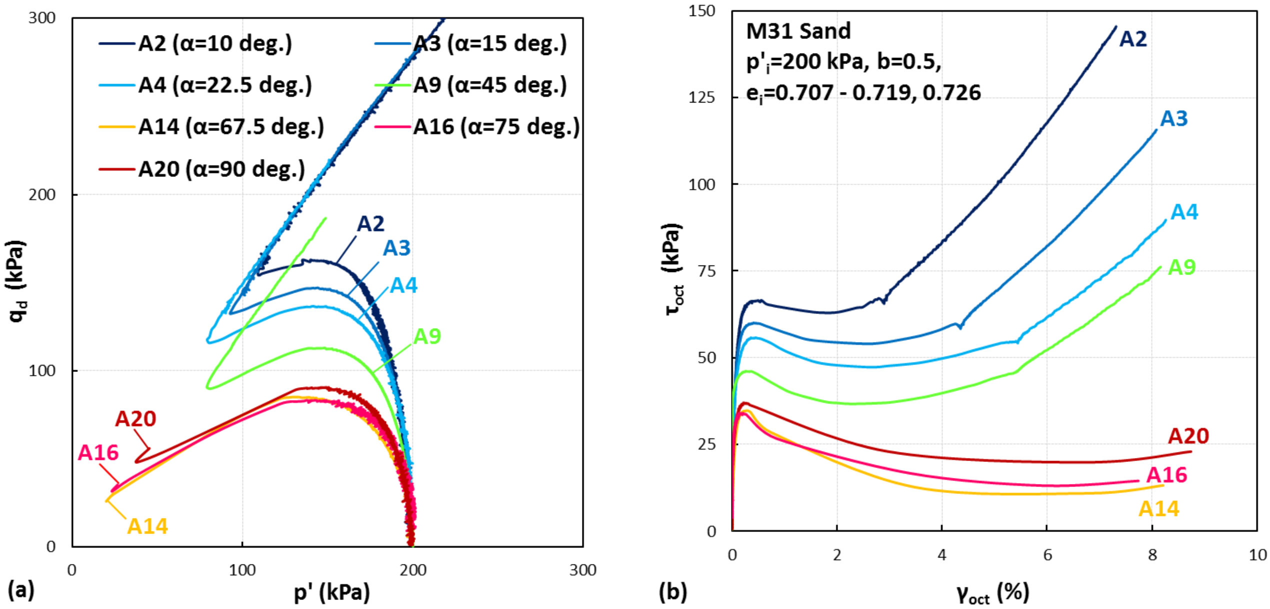


**Σχ. 6** Απόκριση χαλαρής ισότροπα στερεοποιημένης άμμου σε μονοτονική αστράγγιστη φόρτιση με σταθερές $\alpha$, $b$ και $p$ παραμέτρους **a** Ενεργές τασικές οδεύσεις στο $q_d - p'$ επίπεδο. **b** Καμπύλες οκταεδρικής διατμητικής τάσης – παραμόρφωσης ($\tau_{oct} - \gamma_{oct}$)

**Fig. 6** Response of loose IC sand to monotonic undrained loading with constant $\alpha$, $b$ and $p$ parameters **a** Effective stress paths in the $q_d - p'$ plane. **b** Octahedral shear stress – strain curves ($\tau_{oct} - \gamma_{oct}$)

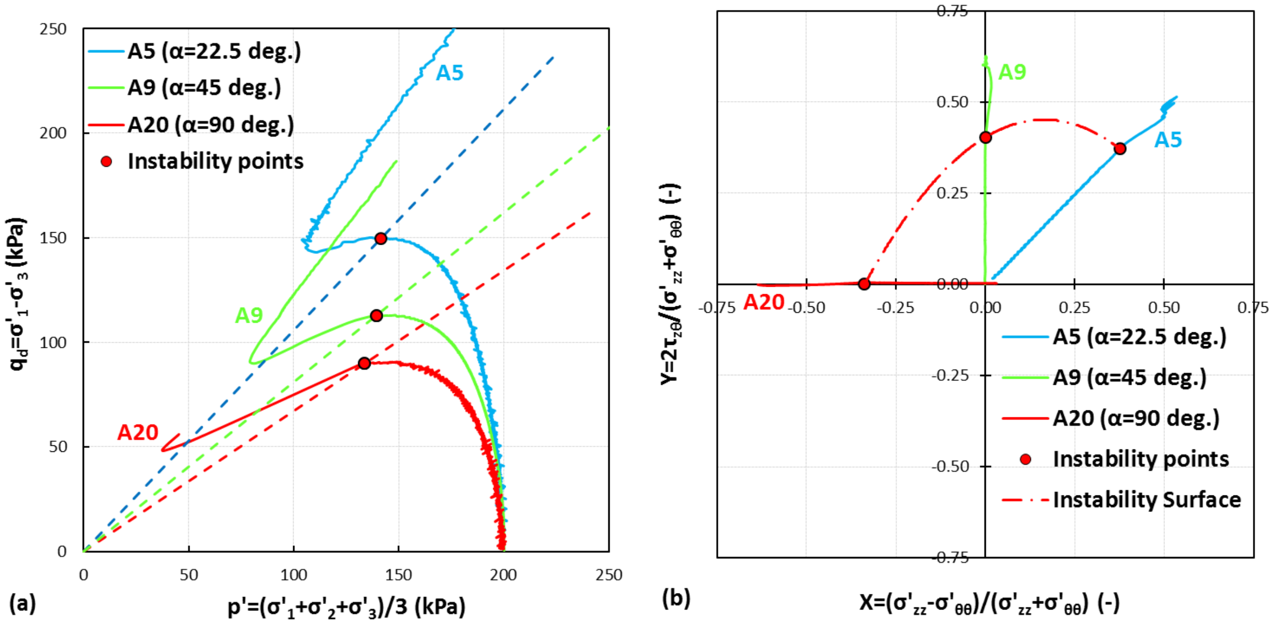


**Σχ. 7** Ορισμός της Τοπικής Οριακής Επιφάνειας, των Γραμμών Αστάθειας και της Επιφάνειας Αστάθειας της χαλαρής ισότροπα στερεοποιημένης άμμου με τη βοήθεια των τασικών οδεύσεων **a** στο $q_d - p'$ επίπεδο και **b** στο $Y - X$ επίπεδο

**Fig. 7** Definition of the Local Boundary Surface (Symes et al. 1984, Sibuya and Hight 1987), Instability Lines (Lade 1993) and Instability Surface (Triantafyllos et al. 2019) of loose isotropically consolidated sand by means of stress paths **a** in the $q_d - p'$ plane and **b** in the $Y - X$ plane

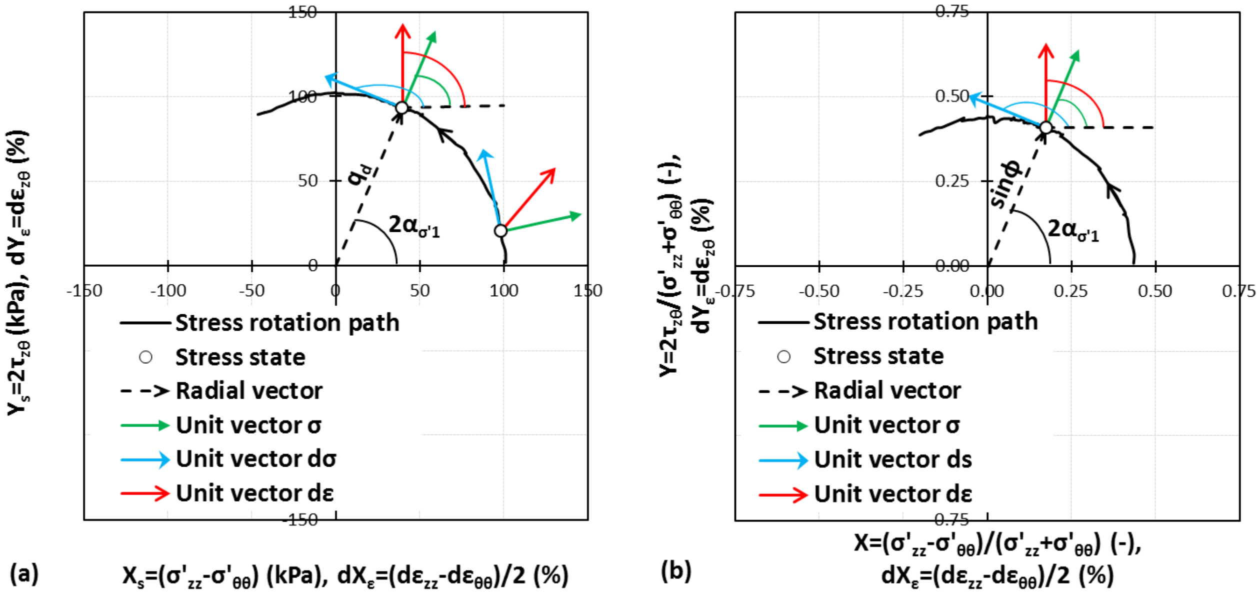


**Σχ. 8** Τασική όδευση που σχετίζεται με στροφή των κύριων αξόνων τάσεως και κύριες κατευθύνσεις τάσεως, **σ**, προσαυξητικής τάσεως, d**σ**, και προσαυξητικής παραμορφώσεως, d**ε**: **a** στο $Y_s - X_s$ επίπεδο και **b** στο $Y - X$ επίπεδο

**Fig. 8** Stress path associated with rotation of the stress principal axes and principal directions of stress, **σ**, incremental stress, d**σ**, and incremental strain, d**ε**: **a** in the $Y_s - X_s$ plane and **b** in the $Y - X$ plane

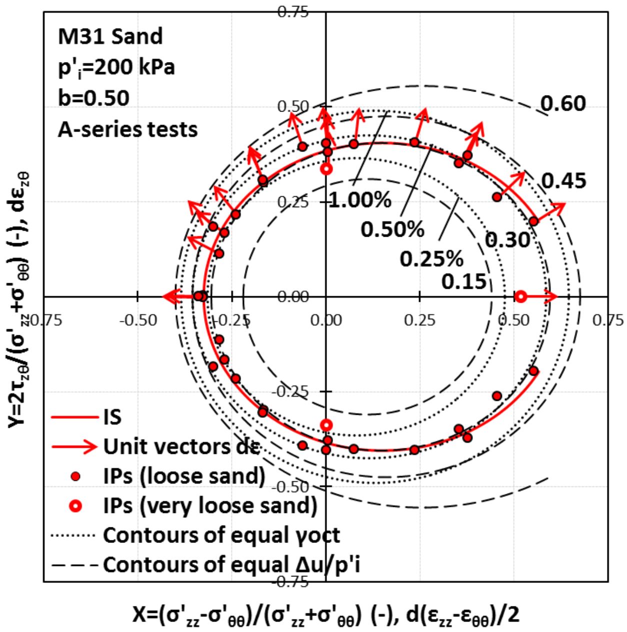


**Σχ. 9** Επιφάνεια αστάθειας της χαλαρής ισότροπα στερεοποιημένης άμμου και περιγράμματα ίσων τιμών $\gamma_{oct}$ και $\Delta u \,/\, p'_{in}$ κατά τη συστολική φάση απόκρισης στο $Y - X$ επίπεδο

**Fig. 9** Instability surface (IS) of loose isotropically consolidated sand and contours of equal $\gamma_{oct}$ and $\Delta u \,/\, p'_{in}$ during the contractive phase of response in the $Y - X$ plane

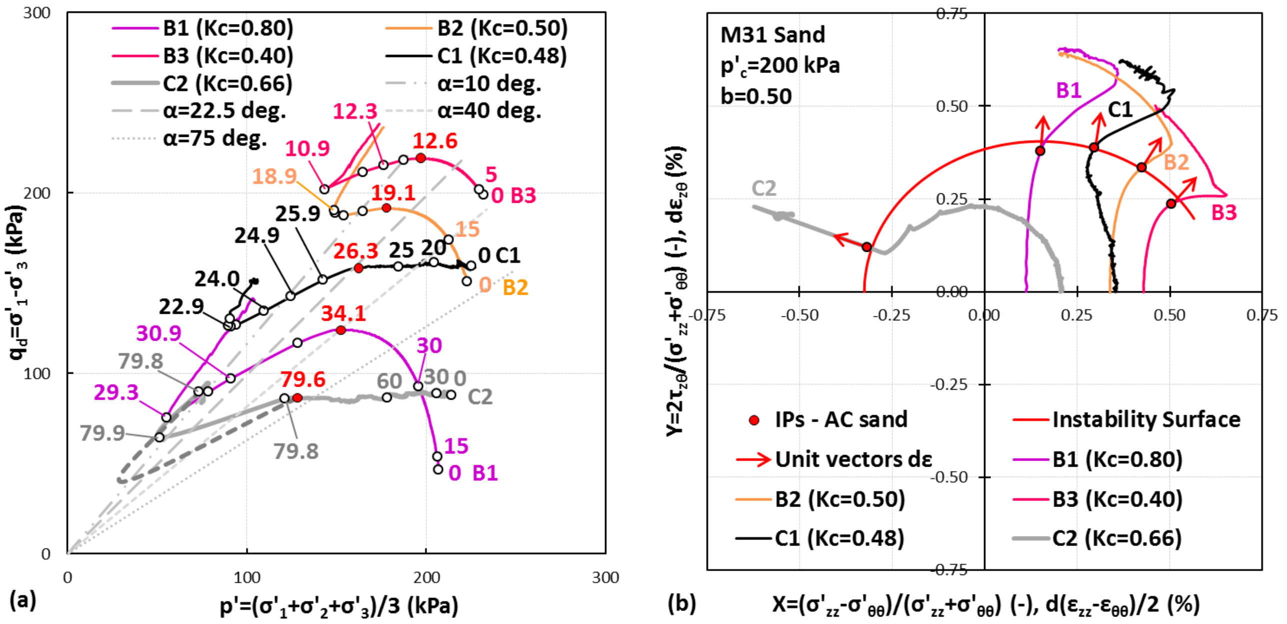


**Σχ. 10** Απόκριση χαλαρής ανισότροπα στερεοποιημένης άμμου σε μονοτονική αστράγγιστη φόρτιση με στροφή των κύριων αξόνων τάσεως και σταθερές $b$ και $p$ παραμέτρους. **a** Ενεργές τασικές οδεύσεις στο $q_d - p'$ επίπεδο. **b** Τασικές οδεύσεις στο $Y - X$ επίπεδο

**Fig. 10** Response of loose AC sand to monotonic undrained loading with rotating stress principal axes and constant $b$ and $p$ parameters. **a** Effective stress paths in the $q_d - p'$ plane. **b** Stress paths in the $Y - X$ plane

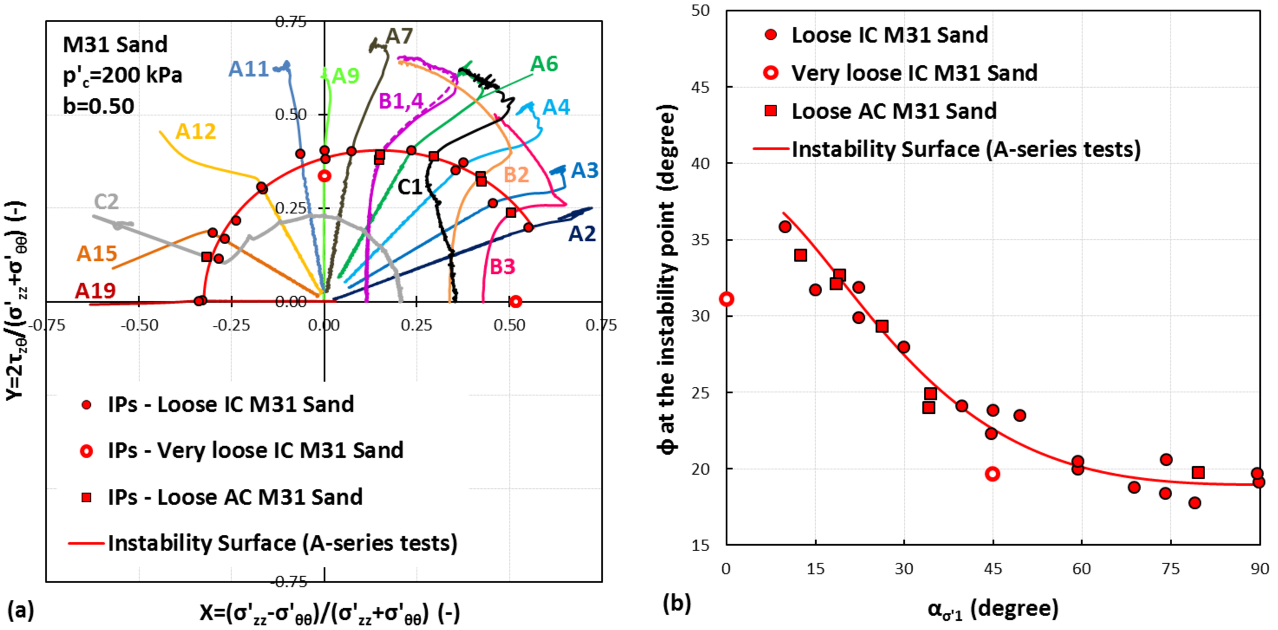


**Σχ. 11** Σημεία αστάθειας χαλαρής άμμου για διαφορετικές ιστορίες στερεοποίησης και αστράγγιστης φόρτισης. **a** Σημεία αστάθειας και τασικές οδεύσεις στο $Y - X$ επίπεδο. **b** Σημεία αστάθειας στο $\varphi - \alpha_{\sigma'1}$ επίπεδο

**Fig. 11** Instability points of loose sand for different histories of consolidation and undrained loading. **a** Instability points and stress paths in the $Y - X$ plane. **b** Instability points in the $\varphi - \alpha_{\sigma'1}$ plane

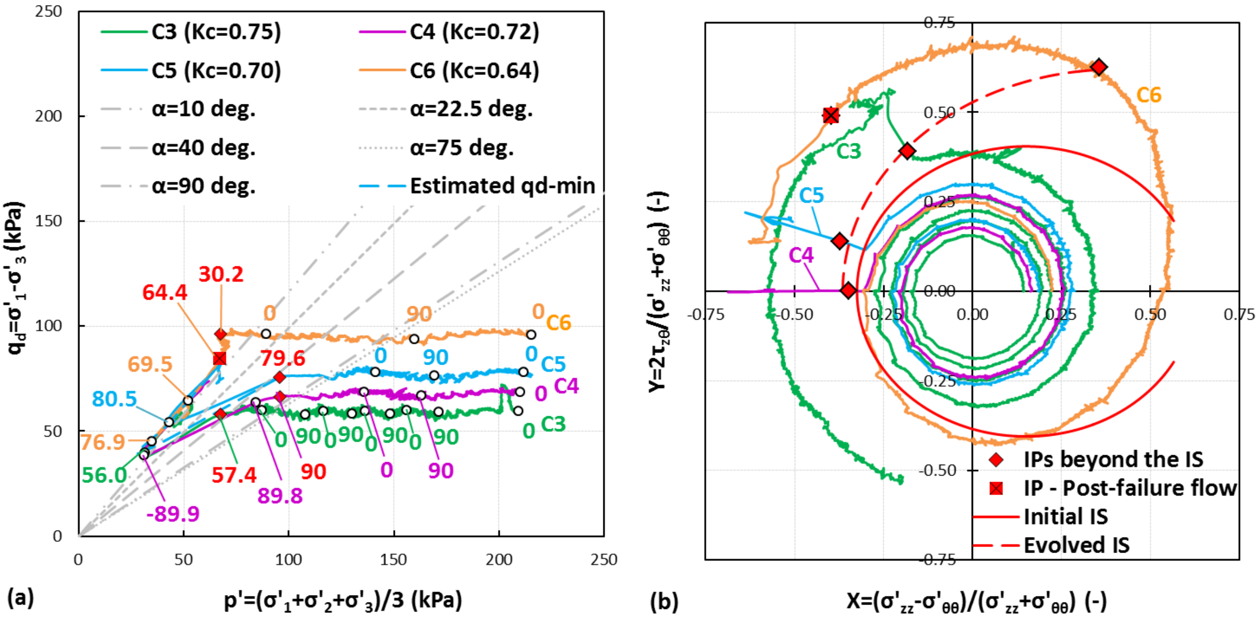


**Σχ. 12** Απόκριση χαλαρής ανισότροπα στερεοποιημένης άμμου σε μονοτονική αστράγγιστη φόρτιση με στροφή των κύριων αξόνων τάσεως και σταθερές $q$, $p$ και $b$ παραμέτρους. **a** Ενεργές τασικές οδεύσεις στο $q_d - p'$ επίπεδο. **b** Τασικές οδεύσεις στο $Y - X$ επίπεδο

**Fig. 12** Response of loose AC sand to monotonic undrained loading with rotating stress principal axes and constant $q$, $p$ and $b$ parameters. **a** Effective stress paths in the $q_d - p'$ plane. **b** Stress paths in the $Y - X$ plane

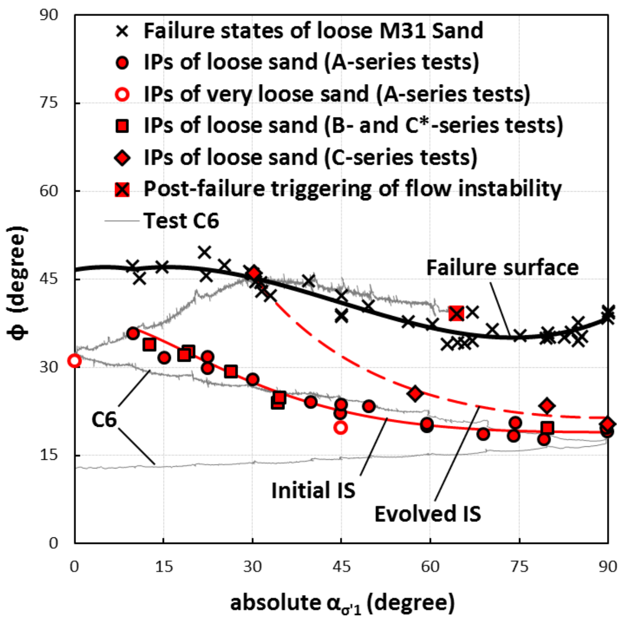


**Σχ. 13** Επίδραση της ιστορίας τάσεων στη συνθήκη αστάθειας χαλαρής άμμου: γωνία διατμητικής αντίστασης, $\varphi$, σε συνάρτηση με τη γωνία κύριας κατεύθυνσης τάσεως, $\alpha_{\sigma'1}$, στα σημεία αστάθειας και κορυφαίας αστοχίας

**Fig. 13** Stress history effects on the flow instability condition of loose sand: mobilised angle of shearing resistance, $\varphi$, against the principal stress direction angle, $\alpha_{\sigma'1}$, at the instability and peak-failure states

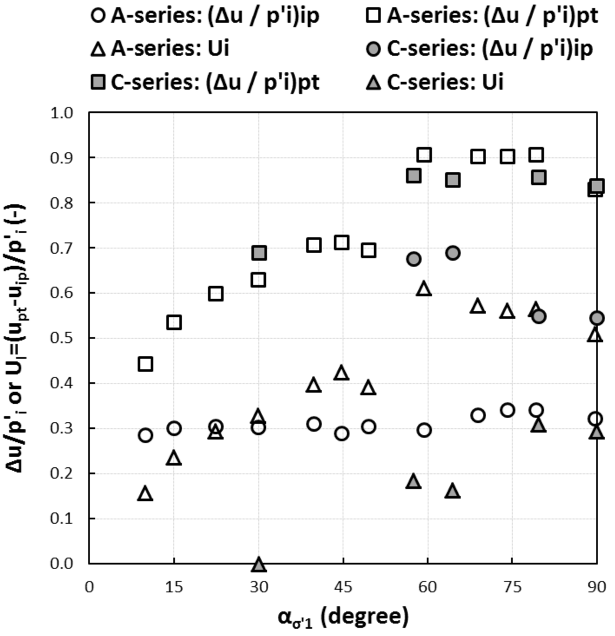


**Σχ. 14** Επίδραση της ιστορίας παραμορφώσεων στη συνθήκη αστάθειας και στη συμπεριφορά της χαλαρής άμμου κατά τη μονότονη ρευστοποίηση: κανονικοποιημένη υπερπίεση του ύδατος πόρων, $\Delta u$ / $p'_{in}$, και παράμετρος μονότονης ρευστοποίησης, $U_I$, σε συνάρτηση με τη γωνία κύριας κατεύθυνσης τάσεως, $\alpha_{\sigma'1}$, στα σημεία αστάθειας και αλλαγής φάσης

**Fig. 14** Strain history effects on the triggering condition and deformation pattern of flow of loose sand: normalised excess pore-water pressure, $\Delta u$ / $p'_{in}$, and flow parameter, $U_I$, against the principal stress direction angle, $\alpha_{\sigma'1}$, at the instability and phase-transformation points

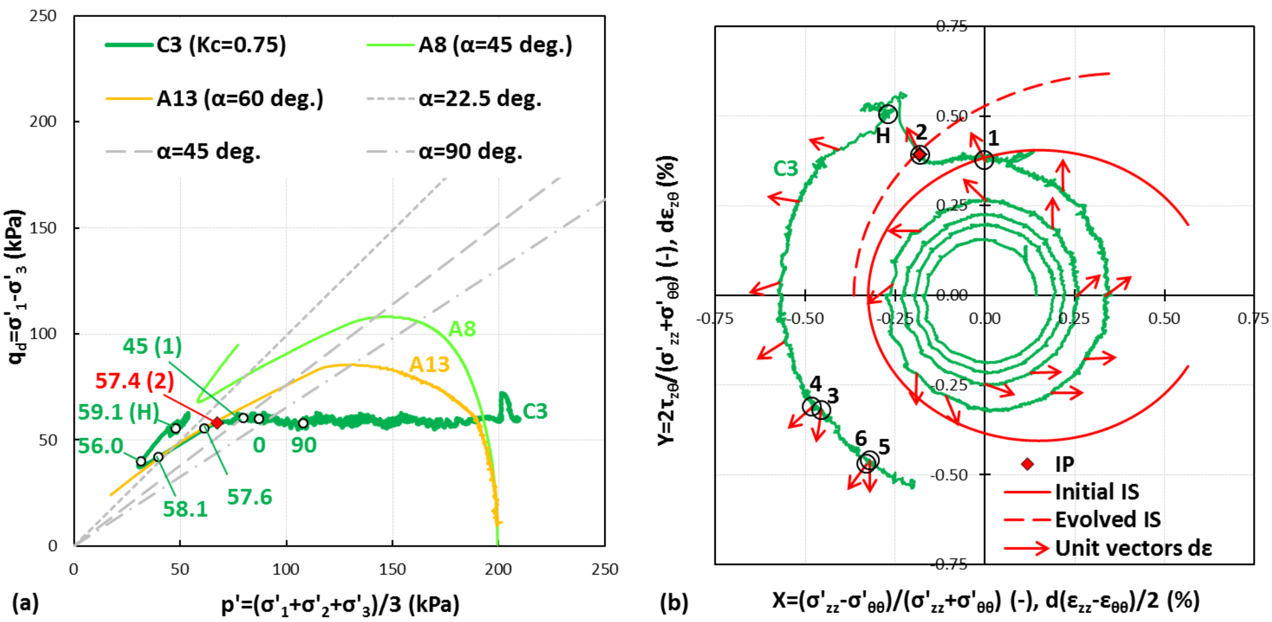


**Σχ. 15** Τασική όδευση από τη δοκιμή C3: **a** στο $q_d - p'$ επίπεδο και **b** στο $Y - X$ επίπεδο

**Fig. 15** Stress path from test C3: **a** in the $q_d - p'$ plane and **b** in the $Y - X$ plane

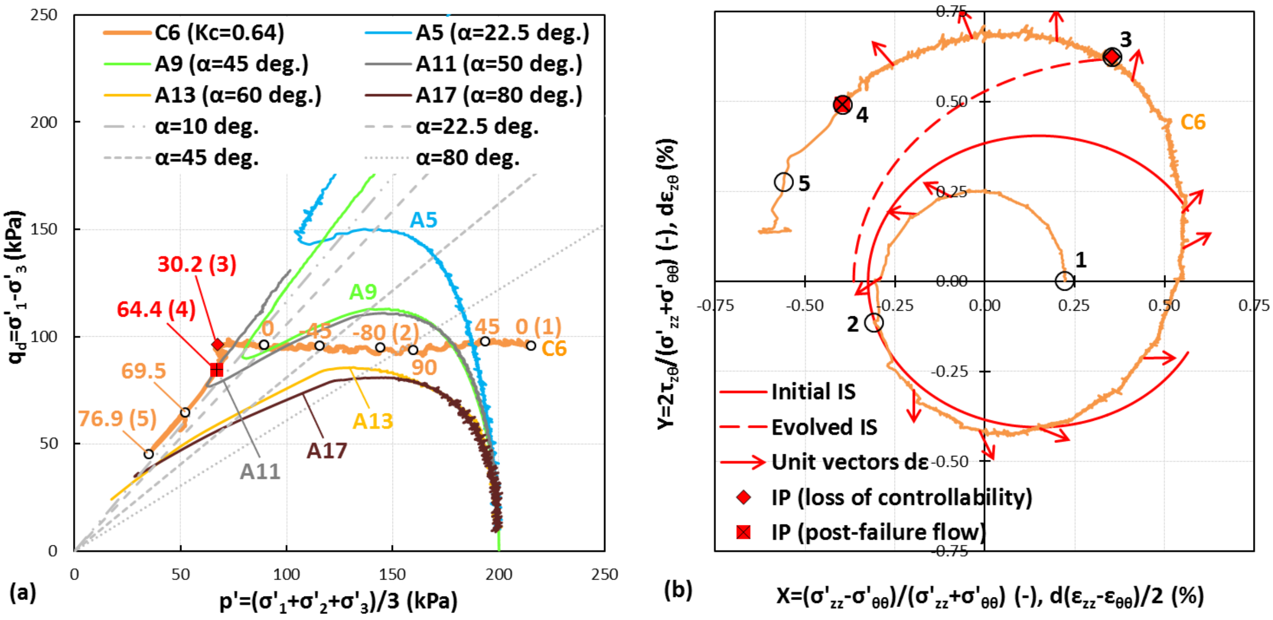

**Σχ. 16** Τασική όδευση από τη δοκιμή C6: **a** στο $q_d - p'$ επίπεδο και **b** στο $Y - X$ επίπεδο

**Fig. 16** Stress path from test C6: **a** in the $q_d - p'$ plane and **b** in the $Y - X$ plane

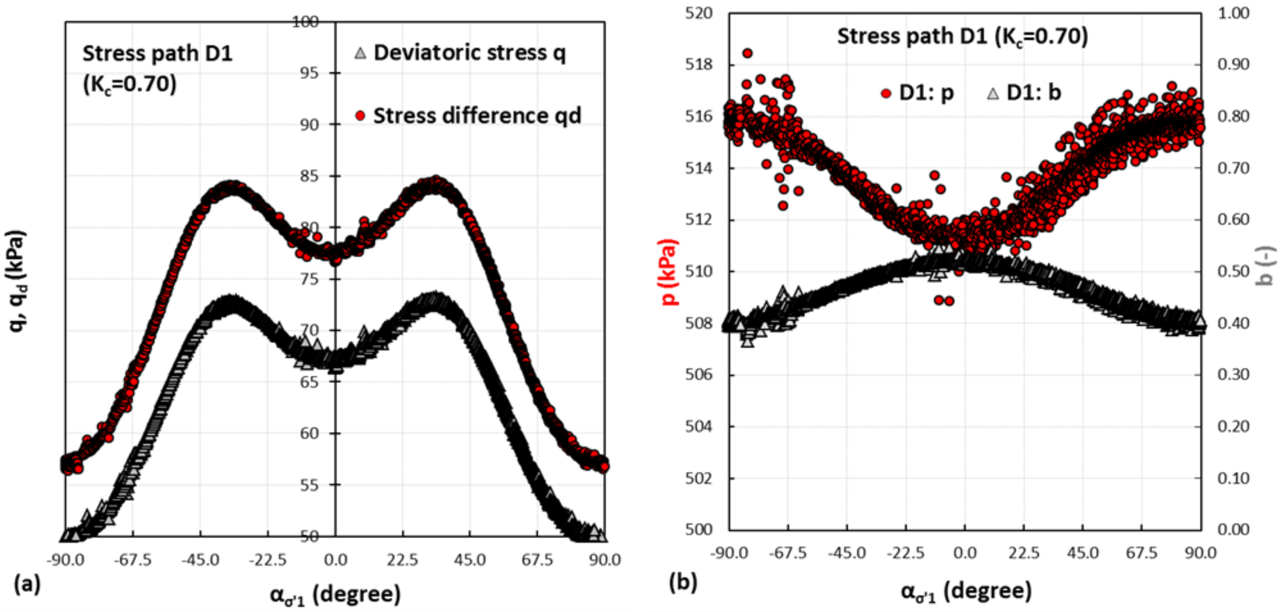

**Σχ. 17** Χαρακτηριστικά της τασικής όδευσης D1. **a** Περιοδική μεταβολή των τάσεων $q$ και $q_d$ με τη γωνία $\alpha_{\sigma'1}$. **b** Περιοδική μεταβολή της τάσης $p$ και της παραμέτρου $b$ με τη γωνία $\alpha_{\sigma'1}$

**Fig. 17** Characteristics of the stress path D1. **a** Periodic change of $q$ and $q_d$ with $\alpha_{\sigma'1}$. **b** Periodic change of $p$ and $b$ with $\alpha_{\sigma'1}$

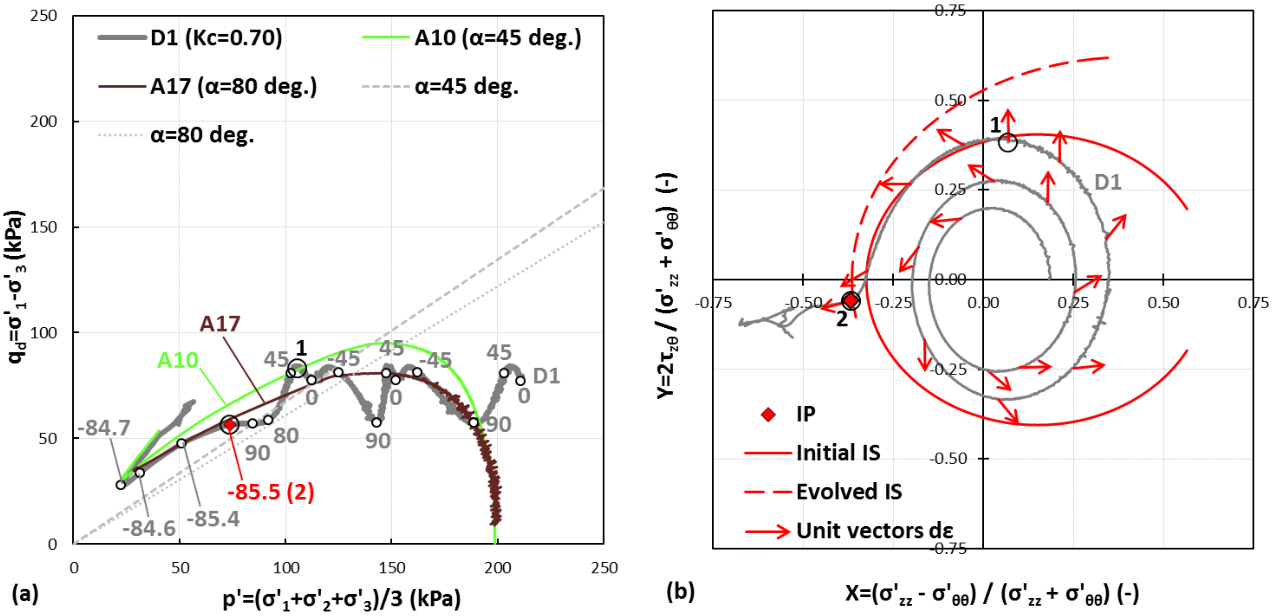


**Σχ. 18** Τασική όδευση από τη δοκιμή D1: **a** στο $q_d - p'$ επίπεδο και **b** στο $Y - X$ επίπεδο

**Fig. 18** Stress path from test D1: **a** in the $q_d - p'$ plane and **b** in the $Y - X$ plane

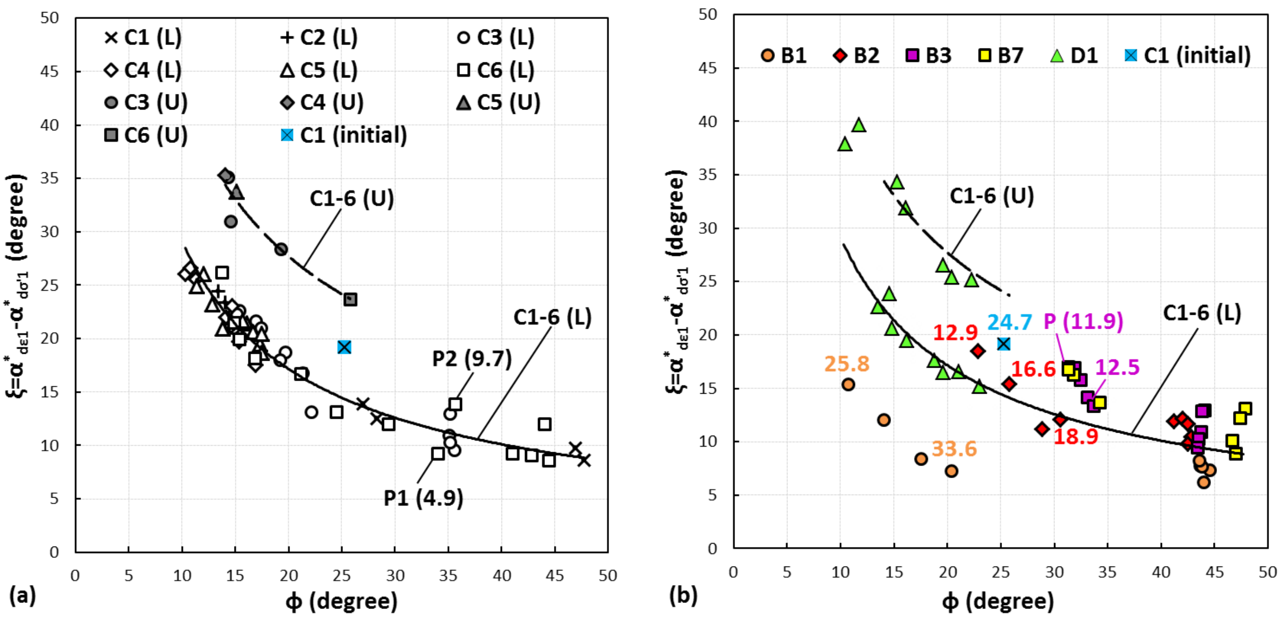


**Σχ. 19** Επίδραση της ιστορίας τάσεων – παραμορφώσεων στη μη ομοαξονική συμπεριφορά της άμμου υπό αστράγγιστη φόρτιση με στροφή των κύριων αξόνων τάσεως. **a** Σχέση μεταξύ των γωνιών $\xi$ και $\varphi$ στις δοκιμές τύπου C. **b** Σχέση μεταξύ των γωνιών $\xi$ και $\varphi$ στις δοκιμές τύπου B και στη δοκιμή D1

**Fig. 19** Stress – strain history effects on the non-coaxiality of sand under undrained loading with rotation of the stress principal axes. **a** Relationship between the angles $\xi$ and $\varphi$ in the C-series tests. **b** Relationship between the angles $\xi$ and $\varphi$ in the B-series tests and in test D1

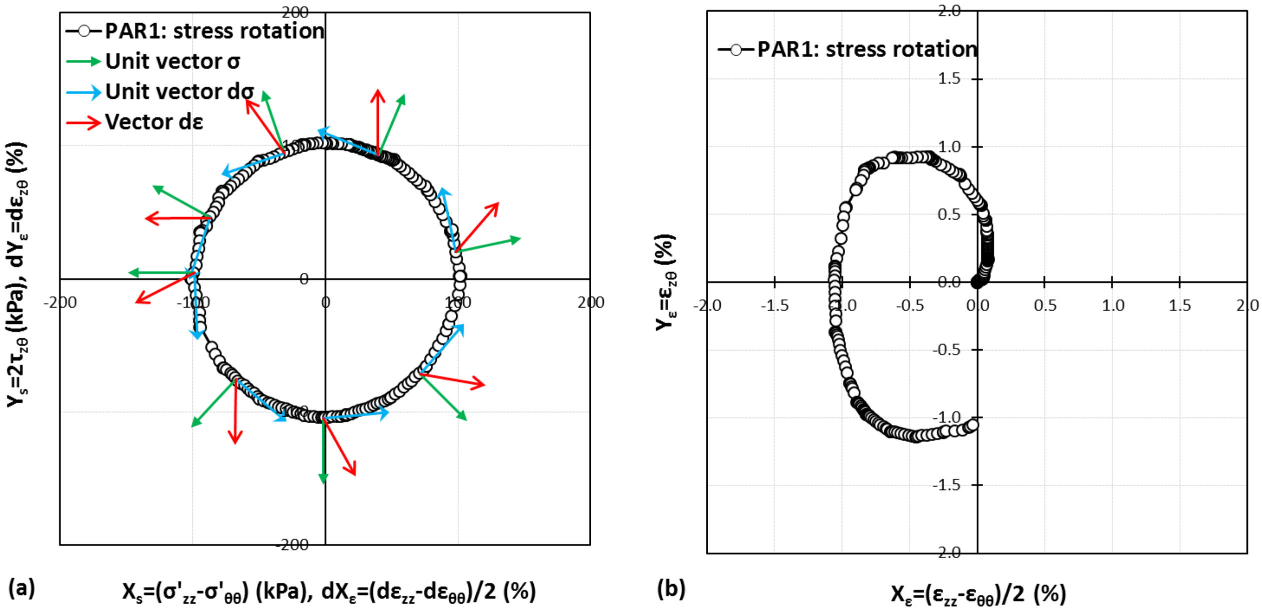


**Fig. 20** Στροφή των κύριων αξόνων τάσεως με σταθερές τις ενεργές κύριες τιμές τάσεως στη δοκιμή PAR1 με $\eta$ = 1.01, $b$ = 0 και $p'$ = 100 kPa. **a** Τασική όδευση στο $Y_s - X_s$ επίπεδο. **b** Όδευση παραμορφώσεως στο $Y_\varepsilon - X_\varepsilon$ επίπεδο

**Fig. 20** Rotation of the stress principal axes at constant effective stress principal values in test PAR1 at $\eta$ = 1.01, $b$ = 0 and $p'$ = 100 kPa. **a** Stress path in the $Y_s - X_s$ plane. **b** Strain path in the $Y_\varepsilon - X_\varepsilon$ plane

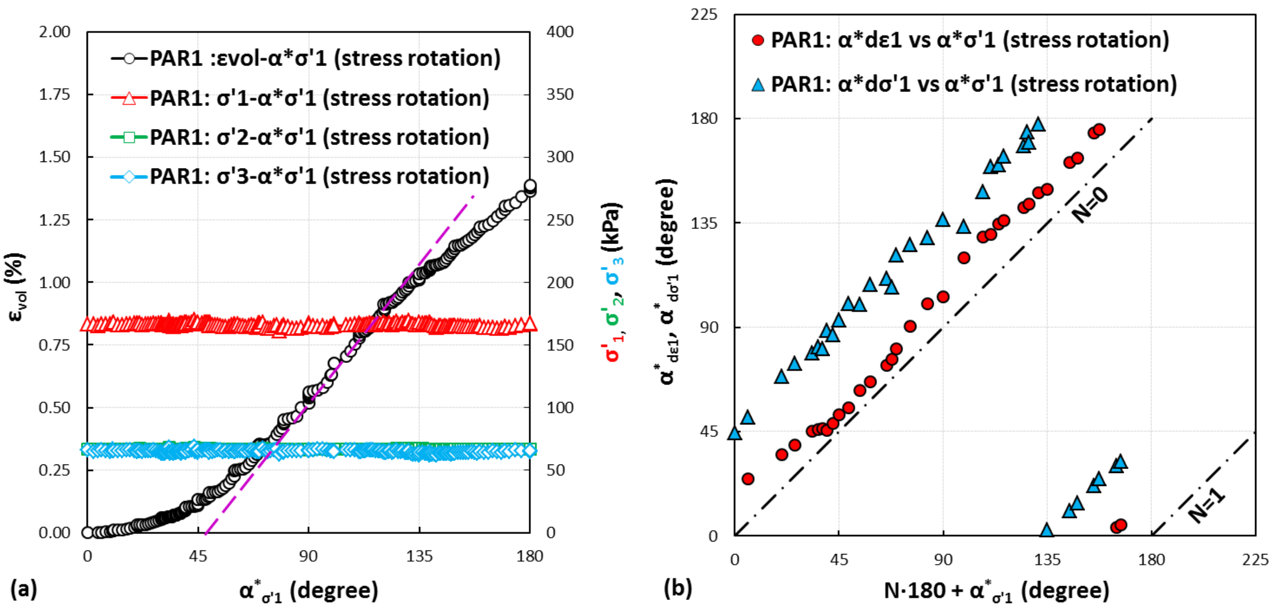


**Fig. 21** Στροφή των κύριων αξόνων τάσεως με σταθερές τις ενεργές κύριες τιμές τάσεως στη δοκιμή PAR1 με $\eta$ = 1.01, $b$ = 0 και $p'$ = 100 kPa. **a** Εξέλιξη των μεγεθών $\varepsilon_{vol}$, $\sigma'_1$, $\sigma'_2$ και $\sigma'_3$ με τη γωνία $\alpha^*_{\sigma'1}$. **b** Εξέλιξη των μεγεθών $\alpha^*_{d\varepsilon1}$ και $\alpha^*_{d\sigma'1}$ με τη γωνία $\alpha^*_{\sigma'1}$

**Fig. 21** Rotation of the stress principal axes at constant effective stress principal values in test PAR1 at $\eta$ = 1.01, $b$ = 0 and $p'$ = 100 kPa. **a** Evolution of $\varepsilon_{vol}$, $\sigma'_1$, $\sigma'_2$ and $\sigma'_3$ with $\alpha^*_{\sigma'1}$. **b** Evolution of $\alpha^*_{d\varepsilon1}$ και $\alpha^*_{d\sigma'1}$ with $\alpha^*_{\sigma'1}$

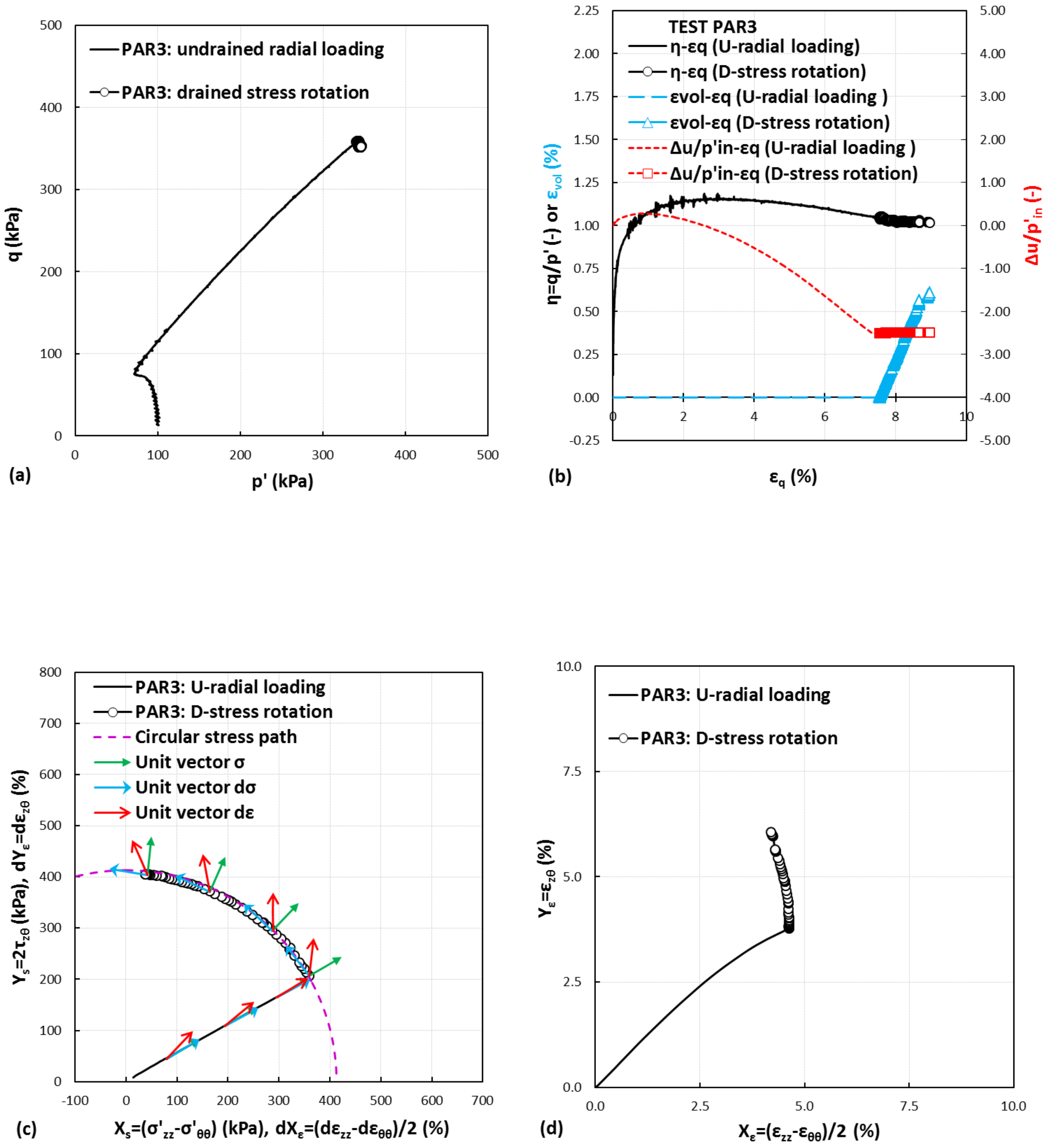


**Fig. 22** Στροφή των κύριων αξόνων τάσεως με σταθερές τις ενεργές κύριες τιμές τάσεως στη δοκιμή PAR3 με $\eta$ = 1.05, $b$ = 0.5 και $p'$ = 343 kPa. **a** Τασική όδευση στο $q - p'$ επίπεδο. **b** Εξέλιξη των μεγεθών $\eta$, $\varepsilon_{vol}$ και $\Delta u / p'_i$ με την παραμόρφωση $\varepsilon_q$. **c** Τασική όδευση στο $Y_s - X_s$ επίπεδο. **d** Όδευση παραμορφώσεως στο $Y_\varepsilon - X_\varepsilon$ επίπεδο

**Fig. 22** Rotation of the stress principal axes at constant effective stress principal values in test PAR3 at $\eta$ = 1.05, $b$ = 0.5 and $p'$ = 343 kPa. **a** Stress path in the $q - p'$ plane. **b** Evolution of $\eta$, $\varepsilon_{vol}$ and $\Delta u / p'_i$ with $\varepsilon_q$. **c** Stress path in the $Y_s - X_s$ plane. **d** Strain path in the $Y_\varepsilon - X_\varepsilon$ plane

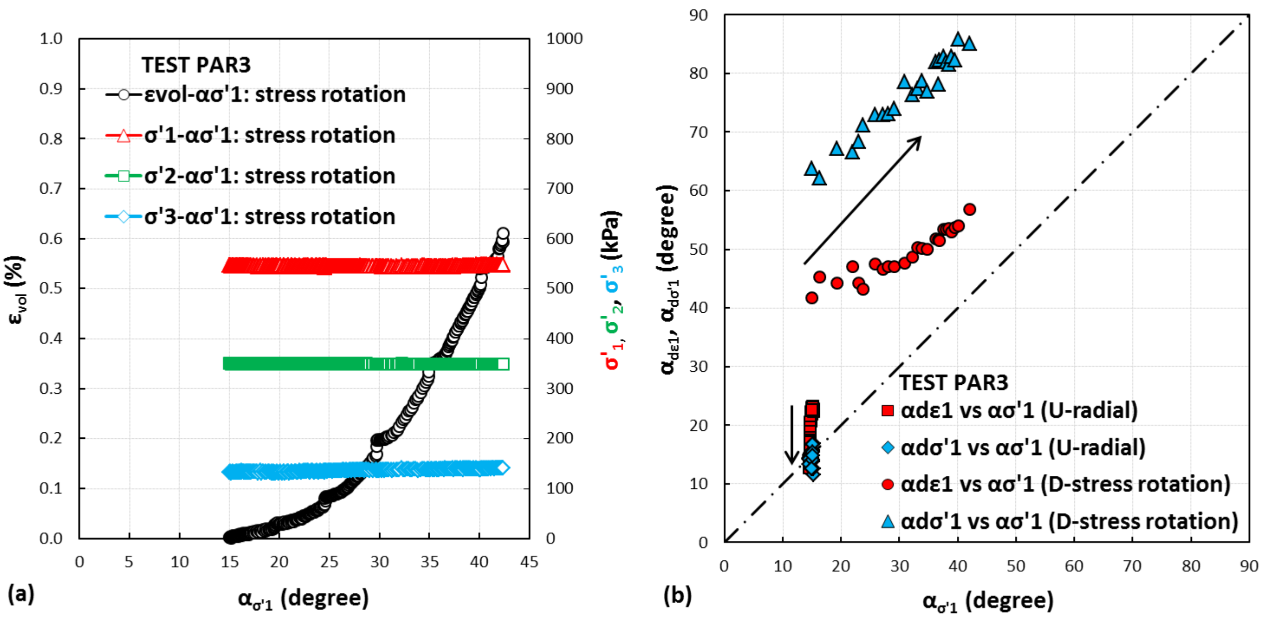


**Fig. 23** Στροφή των κύριων αξόνων τάσεως με σταθερές τις ενεργές κύριες τιμές τάσεως στη δοκιμή PAR3 με $\eta$ = 1.05, $b$ = 0.5 και $p'$ = 343 kPa. **a** Εξέλιξη των μεγεθών $\varepsilon_{vol}$, $\sigma'_1$, $\sigma'_2$ και $\sigma'_3$ με τη γωνία $\alpha^*_{\sigma'1}$. **b** Εξέλιξη των μεγεθών $\alpha^*_{d\varepsilon 1}$ και $\alpha^*_{d\sigma'1}$ με τη γωνία $\alpha^*_{\sigma'1}$

**Fig. 23** Rotation of the stress principal axes at constant effective stress principal values in test PAR3 at $\eta$ = 1.05, $b$ = 0.5 and $p'$ = 343 kPa. **a** Evolution of $\varepsilon_{vol}$, $\sigma'_1$, $\sigma'_2$ and $\sigma'_3$ with $\alpha^*_{\sigma'1}$. **b** Evolution of $\alpha^*_{d\varepsilon 1}$ και $\alpha^*_{d\sigma'1}$ with $\alpha^*_{\sigma'1}$

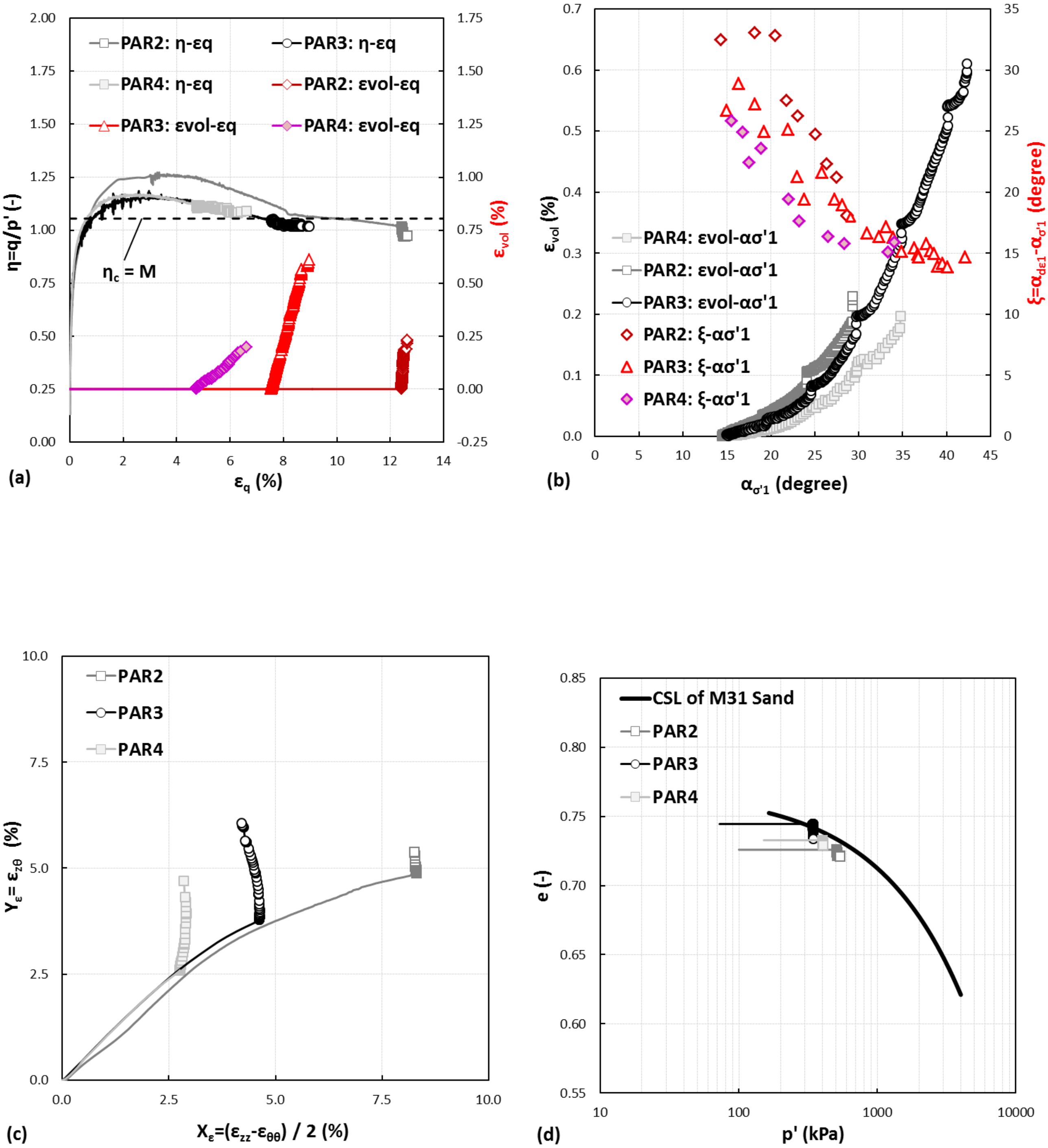


**Σχ. 24** Επίδραση της ιστορίας τάσεων – παραμορφώσεων, πλησιάζοντας την κρίσιμη κατάσταση, στη διαστολικότητα και μη ομοαξονικότητα της άμμου κατά τη στροφή των κύριων αξόνων τάσεως. **a** Εξέλιξη των μεγεθών $\eta$ και $\varepsilon_{vol}$ με την παραμόρφωση $\varepsilon_q$. **b** Εξέλιξη των μεγεθών $\varepsilon_{vol}$ και $\xi$ με τη γωνία $\alpha_{\sigma'1}$. **c** Οδεύσεις παραμορφώσεως στο $Y_\varepsilon - X_\varepsilon$ επίπεδο. **d** Εξέλιξη της κατάστασης της άμμου στο $e - p'$ επίπεδο

**Fig. 24** Stress – strain history effects, nearing critical state, on the dilatancy and non-coaxiality of sand during rotation of the stress principal axes. **a** Evolution of $\eta$ and $\varepsilon_{vol}$ with $\varepsilon_q$. **b** Evolution of $\varepsilon_{vol}$ and $\xi$ with $\alpha_{\sigma'1}$. **c** Strain paths in the $Y_\varepsilon - X_\varepsilon$ plane. **d** Evolution of the state of sand in the $e - p'$ plane

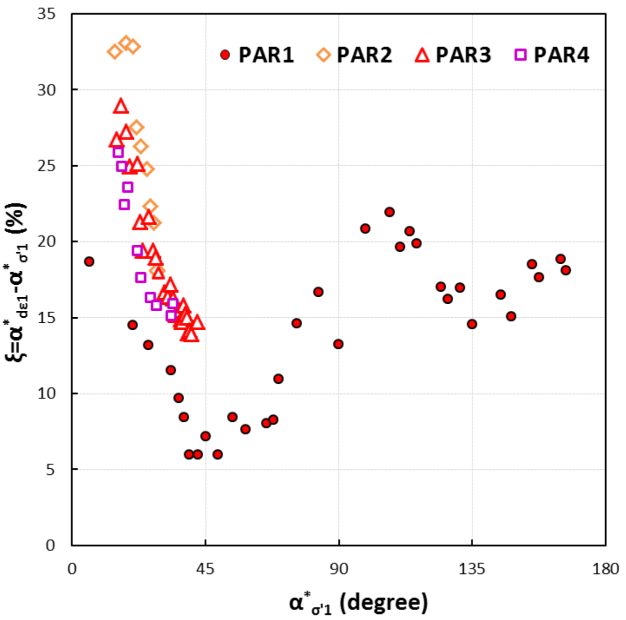


**Σχ. 25** Επίδραση της ιστορίας τάσεων – παραμορφώσεων στη μη ομοαξονικότητα της άμμου κατά τη στροφή των κύριων αξόνων τάσεως με σταθερές ενεργές κύριες τιμές τάσεως: Εξέλιξη της γωνίας $\xi$ με τη γωνία $\alpha^{*}_{\sigma'1}$

**Σχ. 25** Stress – strain history effects on the non-coaxiality of sand under rotation of the stress principal axes at constant effective stress principal values: Evolution of the angle $\xi$ with angle $\alpha^{*}_{\sigma'1}$